Microphysics of the Rapid Development of Heavy Convective Precipitation

Zhaoxia Zeng, Sandra E. Yuter, and Robert A. Houze Jr.

Department of Atmospheric Sciences, University of Washington, Seattle, Washington

David E. Kingsmill

Atmospheric Science Center, Desert Research Institute, Reno, Nevada

ABSTRACT

Two rapidly growing, hail-producing storms observed in Alabama during the Microburst and Severe Thunderstorm project in 1986 were examined: the well-studied single-cell storm case on 20 July 1986 and a single cell within a multicellular storm on 6 July 1986. Both storms are examples of extremely efficient accretional growth processes that produced hail within 10 min. A simple hydrometeor classification algorithm based on multiparameter radar data was used to identify regions within the rain and snow portions of the storm volumes that included hail, graupel, and supercooled rain. By comparing the results of the simple hydrometeor classification algorithm to previous polarimetric analysis and modeling of the 20 July 1986 storm by other authors, the hydrometeor classification methodology for the 6 July 1986 storm was indirectly validated.

The microphysical development of hail and graupel was similar for both the single isolated cell storm and a cell within a multicellular storm. Rapid coalescence within updrafts with high liquid water contents quickly produced precipitation-sized drops that were lofted above the 0°C level and subsequently froze. These frozen drops became hail and graupel embryos and continued to grow by accretion. Supercooled rain was present only in the earliest stages of cell evolution lasting 8–12 min and extending 1–2 km above the 0°C level. Hail and graupel appeared several minutes after the first appearance of supercooled rain. Graupel was present at higher altitudes and encompassed a larger area of the storm than hail. Completion of the glaciation of the supercooled rain and the start of hail and graupel fallout occurred at nearly the same time.

Examination of volumetric statistics of the storms in terms of time–height frequency of hydrometeor type and contoured frequency by altitude diagrams (CFADs) of reflectivity and vertical velocity showed that the evolution of the storm kinematics and microphysics were closely coupled for individual cells. Individual cells can be described in terms of a single particle fountain. Previous studies had shown that in multicellular storms, the ensemble of particle fountains rapidly evolves toward microphysical characteristics indicative of dominant vapor depositional growth, characteristic of stratiform regions, even when strong updrafts are present. This study aided in clarifying that, in contrast to the ensemble of particle fountains, for individual particle fountains the kinematic and microphysical evolution are more closely coupled in time and that vapor depositional growth does not dominate in the individual cell until the updraft associated with the cell has weakened.

In the two cases examined, the combined effects of enhancement of the upper levels of the updraft by the latent heat released by glaciation, and the precipitation loading of the heavy falling particles at lower levels, acted to tear the cell apart at the middle. Previous studies have noted midlevel convergence and constriction of the cell associated with these effects. It is postulated that as a result of these factors, cells producing hail and graupel will hasten their own demise and will have on average shorter lifetimes as distinct cells compared to cells producing only rain.

1. Introduction

Houghton (1968) was one of the first to emphasize the importance of accretion as the primary growth process for hydrometeors in convective storms. Accretion is the general term for collection of cloud water by larger particles sweeping out the cloud water in their paths. Often accretion is further delineated in terms of the hydrometeor type of the larger particle. The collection of cloud water by larger water drops is called coalescence, and collection of cloud water by ice particles is called riming (Rogers and Yau 1989). Coalescence and riming occur most efficiently in the presence of updrafts with magnitudes greater than the fall velocity of the larger drops and ice particles accreting the cloud water. The updraft environment can support high concentrations of cloud water, and the upward advection of particles increases their residence time in cloud, and the opportunity to collect cloud droplets. Accretional growth processes are often defined as convective mi-

Corresponding author address: Professor Sandra Yuter, Department of Atmospheric Sciences, University of Washington, Box 351640, Seattle, WA 98195-1640.
E-mail: yuter@atmos.washington.edu

crophysical processes (Houze 1993, 1997). In contrast, vapor deposition is usually associated with stratiform microphysical processes and can become the dominant microphysical process only when updrafts are absent or sufficiently weak as to not support high concentrations of cloud water.

The life cycle of microphysical processes in precipitating storms has been studied since the first radar observations of precipitating clouds were made (Byers and Braham 1949) but many questions remain. Observational studies by Saunders (1965) and Braham (1964) indicated that simple single-cell clouds have effective lifetimes of typically 20–45 min, about equal to the time required to grow raindrops. Houghton (1968) hypothesized that multicellular storms lasting an hour or more are composed of an ensemble of cells, each with an active lifetime similar to single-cell clouds and with a nearly independent precipitation process, even though some particles may be recycled from one cell to another. Yuter and Houze (1995a–c, hereafter YH) found that the statistical ensemble behavior of the radar echo of a multicellular storm can quickly change from highly heterogeneous convective characteristics indicative of dominant accretional growth to stratiform characteristics indicative of the important role of vapor depositional growth, while the whole storm was still in a kinematically very active stage (i.e., containing strong up- and downdrafts). Questions raised by the YH studies include the following: Why is the period dominated by accretional growth shorter than the period when strong updrafts are present? Is this a characteristic of individual cells as well as the ensemble of cells within the storm? What are the implications of the short period of the microphysically purely convective stage to the evolution of the storm?

Yuter and Houze (1995c) suggested that a multicellular storm can be envisioned as a collection of "particle fountains" with different strengths and of various ages. A particle fountain is associated with a single cell, and consists of a buoyant updraft element and its accompanying precipitation particles and pressure-gradient-forced downdrafts required by mass continuity. The buoyant bubbles first rise and then expand, entraining environmental air, and eventually they lose their buoyancy. In the early stage of the convective region of a multicellular storm, a few young particle fountains are spewing out particles. Soon more particle fountains are present, including both remnants of older particle fountains and newly formed particle fountains. Heavy particles (hail/graupel/big drops) produced by collection of cloud water (coalescence and/or riming) are carried up in the most vigorous fountains. The heavier particles are few and quickly fall out. The vast majority of lighter particles remain and are advected laterally as the bubble expands. They fall out slowly through the weakly buoyant atmosphere created by old bubbles and grow primarily by vapor deposition since cloud water is available at lower concentrations in the weakly buoyant to negatively buoyant environment.

The formation of hail represents an extreme of accretion and hence convective microphysical growth. The hail embryo can be either graupel or frozen drops and some storms exhibit both types (Browning et al. 1976). The relative dominance of each apparently depends on storm intensity and geographic location. Hail embryos of graupel dominate in high plains storms (Dye et al. 1974), while frozen drops are associated with rapid hail development in clouds with lower bases and situations with orographic forcing (Bringi et al. 1996; Hubbert et al. 1998; Petersen et al. 1999).

Three-dimensional, high time resolution polarization radar data indicate certain microphysical properties of precipitation. The presence of hail can be inferred by the combination of high reflectivity (Z) and low differential reflectivity (ZDR) (Bringi et al. 1984; Leitao and Watson 1984). Narrow columnar regions of high positive ZDR that extended up to 2 km above the 0°C level in isolated convective cells are inferred to be due to supercooled raindrops (Hall et al. 1980; Illingworth et al. 1987; among others). In a study of three cells in Florida, Jameson et al. (1996) inferred supercooled raindrops larger than 2-mm diameter above the -7°C level from high ZDR values. Subsequent low-magnitude linear depolarization ratio (LDR) values in the same area indicated that these drops then froze. Bringi et al. (1996, 1997) observed similar columnar features of positive ZDR with a high LDR cap on the inflow side of a hail-producing convective storm. Large numbers of liquid drops were observed from South Dakota School of Mines and Technology (SDSMT) T-28 aircraft penetration in a positive ZDR column and frozen drops were inferred to be the dominant hail embryos. The microphysical interpretation of hail and graupel from dual-polarization data was recently confirmed by El-Magd et al. (2000) in a study comparing multiparameter radar measurements with high-volume in situ measurements obtained on the SDSMT T-28.

In this paper, two rapidly growing convective cells observed in the Microburst and Severe Thunderstorm (MIST) project (Dodge et al. 1986; Wakimoto and Bringi 1988) are examined. The first is a single-cell storm and the second is a cell within a multicellular storm. Both produced hail within 10 min of radar echo detection >10 dBZ and represent examples of extremely efficient accretional growth processes. For the 20 July 1986 single-cell case, we are able to build on a number of other studies examining various aspects of the development of this storm. Wakimoto and Bringi (1988) emphasized the formation of a microburst produced by the storm. They found a narrow shaft of near-zero ZDR associated with a downdraft, which they attributed to the presence of hail. Goodman et al. (1988) studied the lightning and precipitation history of the storm. Their analysis of polarization data suggested that an updraft >20 m s^{-1} transported large drops, initially formed by

coalescence, above the freezing level into a mixed phase zone containing large liquid water content where the ice production rate could be very efficient. Tuttle et al. (1989) also analyzed the polarization radar data and compared results of a 2D model simulation of the storm with observed Z and ZDR data. They proposed that the initial precipitation development was primarily by coalescence but that riming growth became dominant in the rapid precipitation development as the storm evolved. Kingsmill and Wakimoto (1991) studied kinematic, dynamic, and thermodynamic aspects of the storm based on 3D synthesized wind data. They noted two downdrafts: a midlevel downdraft associated with wake entrainment and a lower-level downdraft initiated by precipitation loading that led to the microburst. Additionally, cloud photography revealed a constriction at midlevels associated with a descending reflectivity core and rapid glaciation of the upper levels of the cloud.

We will focus on the development and interaction of supercooled liquid water, graupel, and hail as they relate to the rapid development and demise of the period of dominant accretional growth in the entire storm volume and relate these observations to the particle fountain conceptual model. We will employ a simple hydrometeor identification algorithm based on recognized characteristics of multiple polarization data (Doviak and Zrnic 1993), suited to the limited radar parameter set available during MIST. The algorithm is described in detail in the section 3. The identified hydrometeor types are validated by comparing to the analysis of Goodman et al. (1988) and Tuttle et al. (1989), and examined for physical consistency in the context of the 3D wind field synthesized from Doppler radar data provided by Kingsmill and Wakimoto (1991). We will build on and extend the previous work by addressing whether the behavior of the 20 July 1986 single-cell storm is similar to that of cells within the more commonly occurring multicellular storms in the same region. To the degree the characteristics of hail development are similar between the single-cell and multicellular cases, it will extend the generality of the previous results on the microphysical evolution of hail within storms in this region. The main objective of this study is to use the explicit microphysical information extracted from the polarization data collected in these cases of highly efficient accretional growth to help answer the questions raised by Yuter and Houze to better understand the ensemble behavior of multicellular storms.

2. Data

The multiple polarization radar data used in this study were collected by the National Center for Atmospheric Research's (NCAR) CP-2 radar. The following radar parameters were obtained by CP-2 during MIST: S-band Z, ZDR, and radial velocity, X-band Z, LDR, and radial velocity. The radar was configured to scan sectors over the region of interest and yielded high time and spatial

resolution volumes. Seven volumes from 1400–1435 central daylight time (CDT)[1] were examined for the 20 July 1986 case, and six volumes from 1524–1548 CDT were examined for the 6 July 1986 case. The radar data used in this study were first edited using NCAR SOLO software to unfold radial velocity and to remove ground clutter and apparent spurious data such as sidelobe contaminated echoes (Herzegh and Carbone 1984), flare echoes (Wilson and Reum 1988), and second-trip echoes (Rinehart 1991). The NCAR REORDER software (Oye and Case 1995) was employed to interpolate the radar data fields to a Cartesian grid using a Cressman (1959) interpolation scheme. The Cartesian grid spacing is 0.4 km in the horizontal and 0.5 km in the vertical. As a further quality control step to remove anomalous ZDR data on the edge of the echo, a reflectivity threshold of 10 dBZ was applied such that only data at the grid points that had $Z > 10$ dBZ were retained in the ZDR analysis.

3. Simple hydrometeor identification algorithm

Multiple-polarization radars measure a number of parameters indicative of the size, shape, thermodynamic phase, and spatial orientation of hydrometeors. Enumerable studies have used polarimetric radar parameters to classify hydrometeor types. Such classifications are based on research in polarimetric radar including electromagnetic modeling, field measurements, and aircraft validation. Several investigators have provided summaries of this research in terms of the typical ranges of polarimetric measurements for various forms of precipitation (Doviak and Zrnic 1993; Straka and Zrnic 1993; Straka et al. 2000). However, some categories overlap such that for every set of measured radar variables there is no unique hydrometeor-type mapping.

Overlap among categories usually occurs at the border between hydrometeor types that can be in physical proximity within the storm; for example, the border between regions described as graupel versus hail. From aircraft in situ data, we know that while snow and rain hydrometeor types are often homogenous, graupel and hail are often mixed with rain or snow depending on temperature, and supercooled rain can be mixed with graupel or hail (Bader et al. 1987; El-Magd et al. 2000). Another issue currently obstructing definition of objective criteria for distinguishing where to draw the boundary between hydrometeor types is the lack of accepted definitions for what makes a particle type "dominate" over other types present in the volume in terms of concentrations per liter, or percentage mass, or volume per liter, etc. Both Z and ZDR are weighted by $n_i D_i^6$ where n_i is the number of particles in a particular size range and D is the mean diameter of that size range. Larger particles in the volume will dominate the measured signatures of Z and ZDR. However, how this D^6 weighting

---

[1] Central daylight time = UTC − 5 h.

TABLE 1a. Classification scheme for $T > 0°C$.

Type	Z (dbZ)	ZDR (dB)	Rain boundary
Rain	<55	>0	Inside
Including graupel	40–55	Any	Outside
Including hail	>55	Any	Outside
Ambiguous	<40	<0	Outside

TABLE 1b. Classification scheme for $T < 0°C$.

Type	Z (dBZ)	ZDR (dB)	Rain boundary
Snow	<40	<1	NA
Including graupel	40–55	Any	Outside
Including hail	>55	Any	Outside
Including supercooled rain	15–55	>1	Inside

relates to the descriptions of concentrations typically used by cloud physicists and modelers for realistic drop spectra has only begun to be explored (El-Magd et al. 2000). This ambiguity of mapping for a subset of multiple-parameter space has created difficulties in automating hydrometeor classification. As a result, much of the multiple-polarization-derived hydrometeor classification described in the existing literature has a subjective component when dealing with overlapping categories.

Recent work in neural network and fuzzy logic hydrometeor classification algorithms (Vivekanandan et al. 1999; Liu and Chandrasekar 2000) using multiple polarization data utilize radar parameters that were not available from the CP-2 radar during MIST. To make use of the MIST data, a simple, empirical algorithm is developed to identify a set of basic hydrometeor types. We define "rain" and "snow" as homogenous hydrometeor categories and use mixed hydrometeor categories to portray the in situ observed mixtures of graupel, hail, and supercooled rain with each other and with both rain and snow, depending on temperature. The mixed types below the 0°C level are labeled "including graupel" and "including hail," and those above the 0°C level are labeled "including graupel," "including hail," and "including supercooled rain." The label "including x" indicates a mixture of types where type x is the dominant type in terms of its ability to be sensed by Z and ZDR. For conciseness in the text, we will sometimes drop the including modifier when we are discussing a hydrometeor type but it is implicit whenever we are discussing classified hydrometeor types of graupel, hail, and supercooled rain.

The boundaries between hydrometeor categories are based on values in the literature and held constant. Further, a subset of radar parameter space is defined as "ambiguous" when available information is deemed insufficient to make a classification. The hydrometeor categories and their criteria are shown in Table 1 and Fig. 1. The criteria are an adaptation of previously published work, with the addition of a new method of deriving a rain–hail boundary in Z–ZDR space, described below.

The classification of echo within a three-dimensional volume is determined using four criteria: whether the point is above or below the freezing level based on upper-air sounding data,[2] the Z value, the ZDR value, and whether the point in Z–ZDR space is inside or outside a defined rain boundary. Below the 0°C level, snow and supercooled rain categories cannot exist. Above the 0°C level, rain must be supercooled. Below the 0°C level, an ambiguous category is used for points less than 40 dBZ with ZDR <0 as these points could include small hail, small graupel, and light rain, consisting of primarily small, nearly spherical drops.

An important component of hydrometeor type identification is the ability to distinguish regions that contain

---

[2] We use the environmental 0°C level as an estimate of the freezing level throughout the precipitation region. For an undiluted parcel rising from the surface, the freezing level can be a few kilometers higher than the environmental 0°C level (sections 4a and 5a). Therefore, the classification of supercooled rain has additional uncertainty related to the uncertainty in the actual 0°C level associated with the predominately partially diluted parcels of the storm (Raymond and Blyth 1986). The nature of this uncertainty will tend to overestimate the vertical depth of supercooled rain.
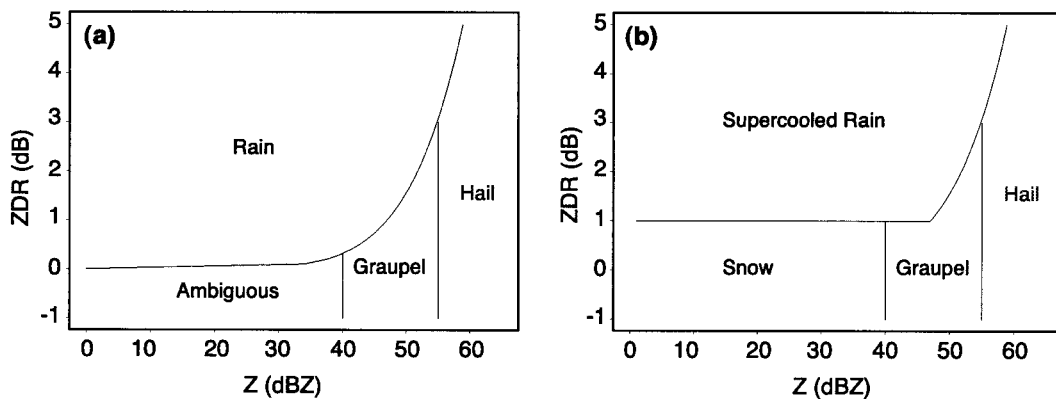

FIG. 1. Schematic of hydrometeor categories in Z–ZDR space for (a) levels below 0°C and (b) above 0°C. See also Table 1.

only rain from regions that contain a mixture of rain and other particles, such as graupel and hail. Neither Z nor ZDR can unambiguously distinguish pure rain from mixtures of rain with graupel/hail. LDR signatures are different in pure rain versus rain mixed with other particles and are sensitive to the density of the dominant particles (El-Magd et al. 2000). However, X-band LDR data is easily contaminated by differential attenuation at horizontal versus vertical polarization (Herzegh and Jameson 1992; Bringi et al. 1996). Differential attenuation acts to shift LDR values toward zero. These propagation effects can make physical interpretation of low-magnitude LDR values (> -25 dB) ambiguous, since low-magnitude LDR can be associated with graupel/hail or with a rain region affected by differential attenuation. Holler et al. (1994) avoided this problem by ignoring regions behind high ZDR regions potentially subject to differential attenuation in his analysis. Bringi et al. (1996) proposed an LDR propagation correction that subtracted the increasing trend of LDR along a radial from the individual LDR values at each range gate. However, an increasing trend in LDR within a reflectivity core can be the result of differential attenuation and/or particle canting, and these two factors are difficult to separate. While rain subject to varying degrees of differential attenuation can be associated with a range of LDR values, LDR values $< \sim -25$ dB (larger absolute magnitudes) are usually only associated with rain below the 0°C level. We establish an empirical rain boundary in Z–ZDR space by exploiting this feature of LDR to distinguish pure rain from rain mixed with graupel/hail. Instead of using the individual LDR value at a point to make a classification, we use the ensemble behavior of the reliable portion of LDR data to define the rain boundary. Use of the ensemble behavior of the reliable portion of LDR follows the spirit of Holler et al.'s exclusion of points subject to differential attenuation in the analysis and circumvents the problematic X-band LDR propagation correction that would be necessary if LDR data at each point were used in the classification.

The well-behaved ensemble behavior of LDR values < -25 dB is indicated in Fig. 2a, using data from 1418 CDT on 20 July 1986. The rain-only data are present within a subset region of Z–ZDR space defined to the left of the curve. In contrast, LDR values > -25 dB that include those subject to differential attenuation extend over a wider area on both sides of the curve (Fig. 2b). The choice of LDR = 25 dB as the threshold to distinguish rain-only points is based on the scattering model computation by Bringi et al. (1986) and a variety of observational studies (Jameson and Johnson 1990; Herzegh and Jameson 1992; Chandrasekar and Keeler 1993; Bringi et al. 1996). The curve for the rain boundary was fitted by eye and is approximated by

$$Z = 47(\text{ZDR})^{1.4}. \qquad (1)$$

The curve is tested in Figs. 3 and 4 by comparing data from an earlier and later stage of the same storm when
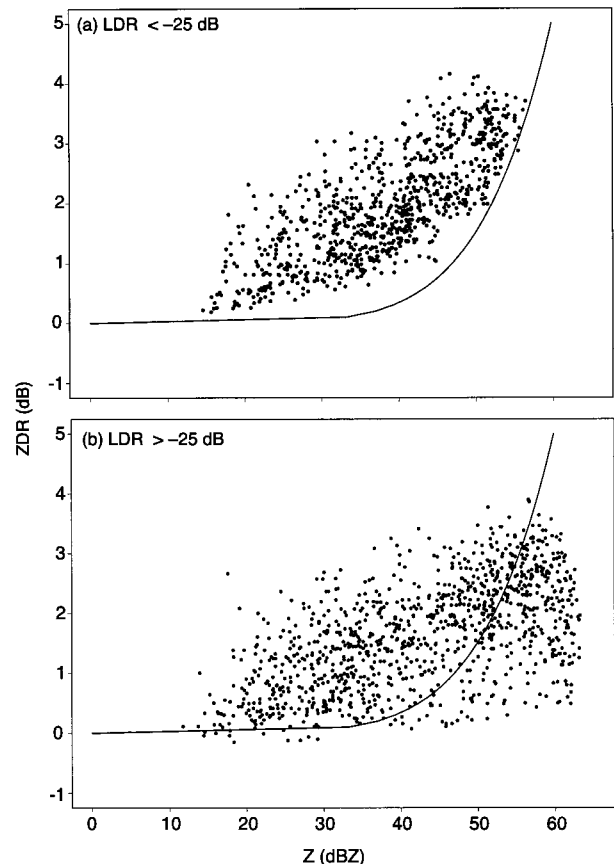

FIG. 2. Scatterplot of Z vs ZDR below the 0°C level. Data points are from an interpolated radar volume at 1418 CDT 20 Jul 1986 in MIST. The curve represents the rain boundary (see text).

the hydrometeors are expected from storm evolution considerations to be almost exclusively rain and from a shallow convective case from MIST on 12 July 1986 when hail was not observed. In all six of these radar volumes, points outside the rain boundary are rare. For the independent data in Fig. 4, 99% of the points were within the rain boundary.

The rain boundary derived using the ensemble characteristics of LDR < -25 dB is similar to rain boundaries in Z–ZDR space obtained from other investigators (Fig. 5). Leitao and Watson (1984) derived a rain boundary by plotting the frequency of occurrence of each Z–ZDR pair from data from less convectively active storms with a high freezing level. Aydin et al. (1986) derived their rain boundary using disdrometer drop-size distributions as input to an electromagnetic scattering model. Assumptions in the model regarding shape, axis ratio, wind shear, evaporation, and temperature can contribute to significant differences between modeled rain and observed rain. Aydin et al. pointed out that discounting less than 1% of Leitao and Watson's observations would displace their curve by as much as 5 dB. Given the uncertainties in modeling and measurement, the LDR-derived rain boundary in (1) is a reasonable approxi-
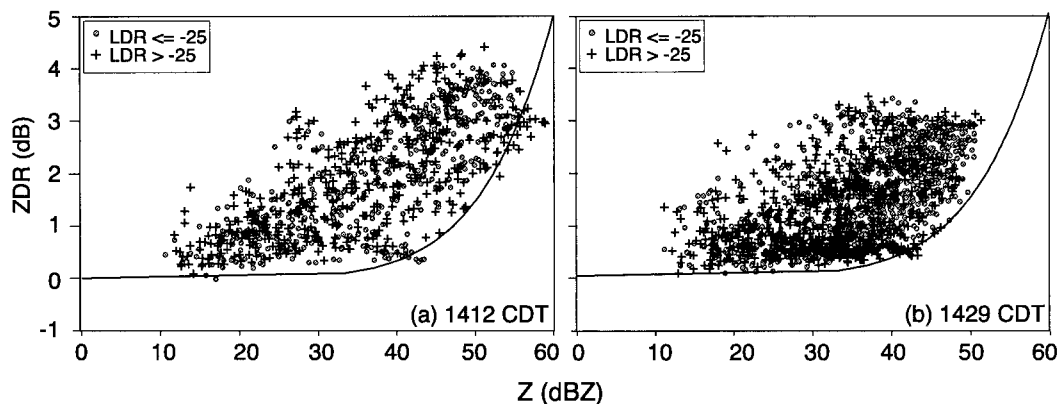
FIG. 3. Scatterplot of Z vs ZDR below the 0°C level at (a) early (prehail) and (b) late (posthail) stages of the same convective storm in Fig. 2.

mation for our purposes to distinguish regions of pure rain from those containing graupel and hail.

4. Hail-producing, single-cell storm on 20 July 1986

Just before 1400 CDT on 20 July 1986, an isolated storm formed 20 km southeast of the CP-2 radar. Its echo reached a height of 14 km within several minutes, and it produced heavy rain, pea-sized hail, and a microburst (Wakimoto and Bringi 1988). The sounding from Redstone, Alabama, launched at 1300 CDT is shown in Fig. 6. This sounding was obtained approximately an hour before the initiation of convection from a location about 20 km south and southeast of where the storm occurred. The sounding was dry adiabatic from the surface to 800 mb. The surface mixing ratio was 17.8 g kg^{-1}. The lifting condensation level (LCL) was at 1.5 km and the CAPE was 2780 J kg^{-1}. An undiluted parcel ascending from the surface would have reached 0°C at a level 1.2 km higher than the environment 0°C level (4.8 km). The level of zero buoyancy was at 150 mb (about 14.3 km MSL). The adiabatic liquid water of the undiluted parcel at 500 mb would be 8.8 g kg^{-1} or 5.6 g m^{-3}. A detailed discussion of the synoptic setting for this case is provided in Wakimoto and Bringi (1988).

a. Cross-section analysis

At 1400 CDT (Fig. 7), the storm was in an early stage of development. Maximum reflectivity of 40–45 dBZ was at 4–4.5-km altitude (Fig. 7b). The region of ZDR >1.5 dB coincided with an area of reflectivity >45 dBZ indicating that the reflectivity core consisted of raindrops with median mass-weighted diameter[3] of >1.8 mm (Seliga and Bringi 1976; Bringi and Chandrasekar

_____
[3] Based on Bringi and Chandrasekar's (2000) relation of S-band ZDR to mass-weighted drop median diameter, $D_0 = 1.529$ ZDR$^{0.467}$.

2000). The contour of ZDR = 1.5 dB extended to a height of 6 km, 1 km above the 0°C level. LDR had values of <−26 dB (not shown) above the 0°C level, indicating that at this initial stage, supercooled rain was present (Figs. 7c,d). A vertical cross section through the centers of the reflectivity maxima (Fig. 7d) shows that the supercooled rain extended to 6 km. We concur with the conclusion of Tuttle et al. (1989), based on the height of the first echo, the visual cloud height, and the positive ZDR column, that the formation of the initial precipitation core was dominated by coalescence.

Six minutes later (1406 CDT), the two reflectivity maxima present at 1400 CDT had merged into one and the storm had intensified (Fig. 8). Within 6 min, the top of the 30-dBZ contour had risen from 5 to 10 km (cf. Fig. 8b and Fig. 7b). A 50-dBZ region (Fig. 8b), which was not present at 1400 CDT, extended to 8-km altitude. A maximum of reflectivity (>55 dBZ) was at 7.5-km altitude. Associated with the Z > 55 dBZ was a very strong LDR center with values ranging from −18 to −13 dB (not shown), indicating a substantial depolarization signal caused by either frozen drops (Smith et al. 1999) or tumbling irregular-shaped hail (Herzegh and Jameson 1992; Bringi et al. 1997). The accompanying ZDR values in the core ranged from 0.5 to 2.5 dB (Fig. 8b). The combination of high Z, low-magnitude LDR, and weak-to-moderate ZDR signatures on the top of the cell strongly suggests coexistence of liquid water and hail. Just below the high Z core at 4–6-km altitude, the ZDR field indicates values of greater than 4.0 dB. The LDR associated with the ZDR maximum had values ranging from −23 to −28 dB (not shown), suggesting mostly liquid water composition. The hydrometeor types determined by the algorithm are shown in Fig. 8d. Hail is indicated inside the reflectivity core where ZDR values are lower. Supercooled water is shown underneath the hail and to the left. Synthesized vertical velocity (Figs. 8c,d) and horizontal wind (Fig. 8c) show an updraft entering from the left side of the cell and slanting slightly upward. The vertical velocity center is
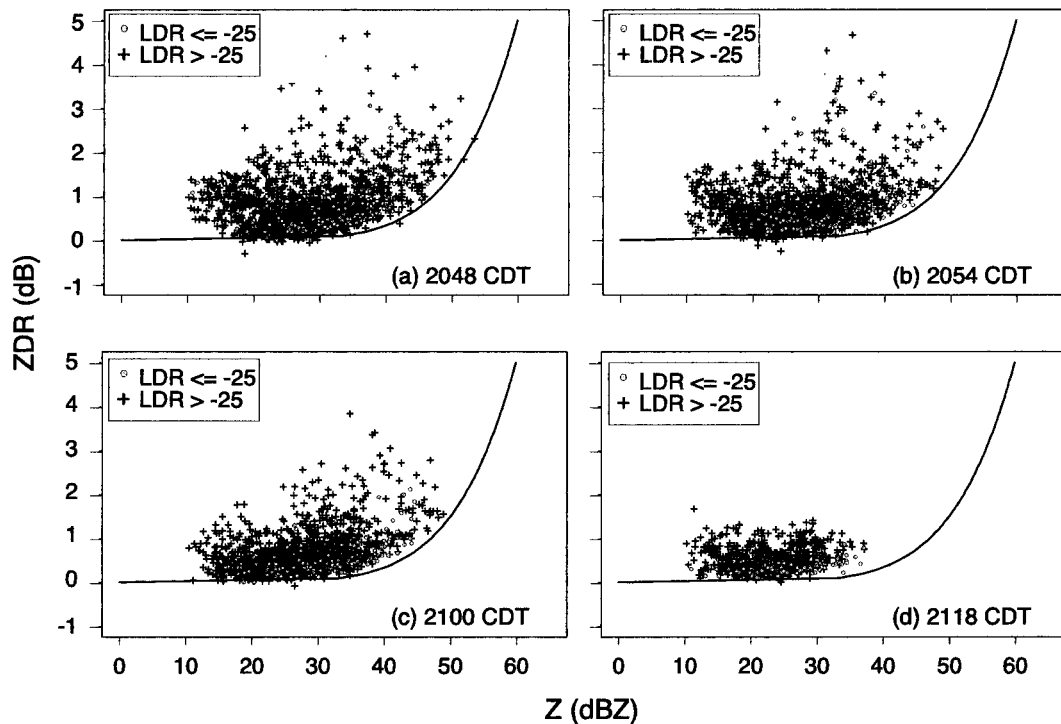
FIG. 4. Scatterplots of Z vs ZDR below 0°C level from the 12 Jul 1986 case obtained in MIST.

collocated with the supercooled water, and hail is present on top of the updraft within a region with velocities of 8–14 m s^{-1}. Graupel indicated by orange is present above the hail column.

Hail formed rapidly during the 6 min between 1400 and 1406. A hail embryo can be a heavily rimed ice crystal or frozen drop. Riming of small ice crystals is too slow to be responsible for the formation of hail within 6 min. We agree with the conclusion of previous authors investigating this storm that the more plausible origin for the initial hail embryos would be large drops

FIG. 5. Comparison of the rain boundary in Z–ZDR space derived in this study with the rain boundaries derived by Leitao and Watson (1984) and Aydin et al. (1986).

that formed by coalescence of liquid water below 6-km altitude, rose, froze into large drops, and continued to collect small cloud droplets. The location of hail above the supercooled rain is consistent with the frozen drop scenario (Fig. 8d). The classification of the hydrometeor algorithm is consistent with the inferred hydrometeor types of Tuttle et al. (1989) and Goodman et al. (1988).

Cross sections through the center of the southern cell at 1412 (Fig. 9) show that the cell continued to rise, with the top of the 30-dBZ contour reaching 13 km. A reflectivity core >50 dBZ extended from 2- to 10-km altitude (Fig. 9b). The maximum reflectivity was 65–70 dB. Collocated with the maximum reflectivity center at 6–8 km was an LDR region with values between −17 and −11 dB (not shown) suggesting irregular-shaped, canting, or tumbling particles inside the core. The ZDR values corresponding to the 55-dBZ contour (Fig. 9b) were negative from 6 to 10 km in the top half of the core, indicating hail or graupel (Illingworth et al. 1987; Bringi et al. 1986; Husson and Pointin 1989). The ample supercooled water at 6–8-km altitude indicated by large positive ZDR values at 1406 (Figs. 8b,d) had glaciated in the 6 min between 1406 and 1412 CDT (Figs. 8 and 9). The rapidly growing echo top during this time suggests that the latent heat released during the glaciation of supercooled water may have played a role in the rapid growth of the upper portion of the cell (Cotton and Anthes 1989).

Doppler wind synthesis from Kingsmill and Wakimoto (1991) identified the location of updraft inflow
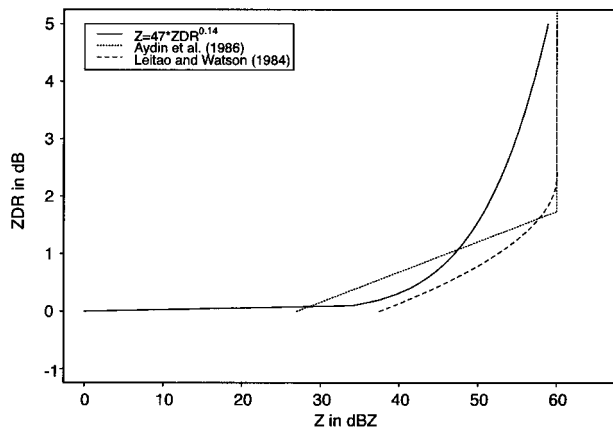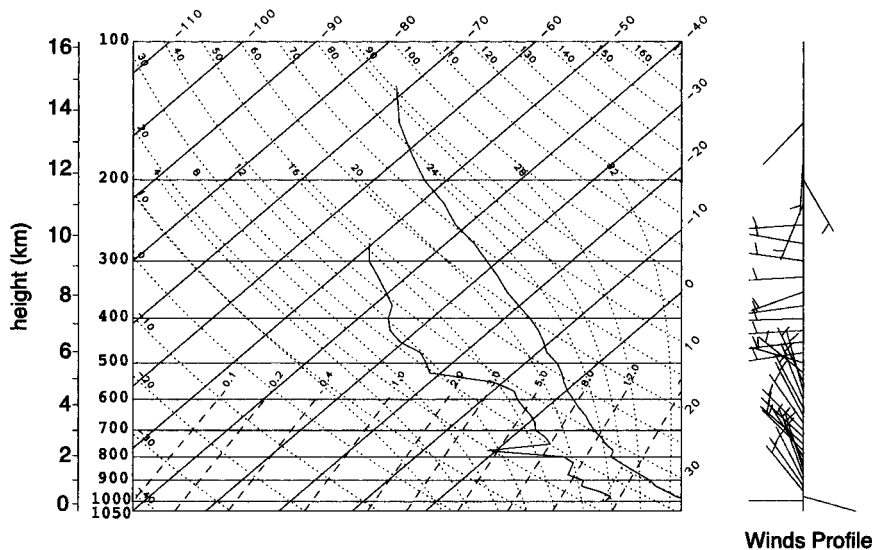
FIG. 6. Environmental sounding taken from Redstone, AL, at 1300 CDT 20 Jul 1986. Solid lines show temperature and dewpoint. Dashed lines are saturation mixing ratio. Dotted curves are the dry and moist adiabats. Wind barbs are at 25-hPa intervals. Full barb is 10 m s^{-1}.

from 2 to 3 km on the northwest side of the cell (Fig. 9c). The updraft is slightly tilted toward the southeast (Fig. 9d), with a maximum magnitude of 12 m s^{-1} centered at 8-km altitude. (The maximum speed of updraft in the volume of this time is about 25 m s^{-1} at 11 km, at a slightly different cross section than the one shown here.) The tilt of updraft in this case is very minor because of the weak vertical wind shear. The reflectivity pattern had a small notch (Fig. 9b) in the location of inflow. The inferred hydrometeor type information (Fig. 9d) reveals a shallow layer of supercooled rain on the updraft side of the cell. Hail was identified inside the high reflectivity core up to 10-km altitude. The bottom of the hail region sank toward the surface compared to its position at 1406 CDT. A small hail region slightly below 0°C level on the southwest side was associated with an area of negative vertical velocity near the surface. The ZDR region >3.5 dB (Fig. 9b), located just under the reflectivity core from 3 km down to the surface, appears to have been caused by the melting of hail into large raindrops.

By 1418 CDT, the core of high reflectivity had descended dramatically (Fig. 10b). The bottom boundary of the 55-dBZ contour had descended to the ground and the upper boundary of the 55-dBZ contour lowered to 6-km altitude. The collapse of the updraft in the center of the cell implied by the descent of the reflectivity core is corroborated by the weakened vertical velocity (Fig. 10d). Noteworthy is that on the west side of the cell, where strong updraft inflow was located at 1412 CDT (Figs. 9c,d), a positive ZDR column (indicating raindrops) was still present with positive ZDR values above the 0°C level (Fig. 10b) and ZDR values >3 dB indicating drops with median mass-weighted diameter of >2.5 mm (Bringi and Chandrasekar 2000) at 2-km al-

titude on the updraft side. In contrast, on the east side of the cell, the 0.5-dB ZDR contour was horizontal at 4-km height, depicting a clear boundary between ice and water. The elevated positive ZDR contours on the west side of the cell indicate that the updraft was still active in parts of the cell despite the overall collapse of the cell owing to the drag of hail and/or graupel. This interpretation is consistent with the synthesized vertical velocity. The 6-km deep hail region at 1412 had descended and collapsed into a shallower layer by 1418 (Fig. 10d). The vertical velocity was only 0–4 m s^{-1} in the hail region, with negative values beneath the hail. Despite the dramatic fallout of the hail region in the middle to lower levels, the graupel region remained in the upper levels, suspended by vertical velocities up to ~8 m s^{-1} (Fig. 10d).

At 1424, the decay of the updraft continued (Fig. 11d). By now the west side of the cell had also collapsed (Fig. 11b). The ZDR contour of 0.5 dB had descended to 4.5 km (Fig. 11b). The LDR values near the ground showed a widespread weak-to-moderate depolarization signal (not shown), indicating probably incompletely melted graupel/hail in the precipitation. The synthesized horizontal wind (Fig. 11c) clearly showed divergent microburst winds at the surface, as shown by Wakimoto and Bringi (1988). The "hole" found by Wakimoto and Bringi is smoothed out in Fig. 11b, since the scale of the microburst is only about 200–300 m wide, which is less than our interpolation grid scale (400 m). The hydrometeor classification (Fig. 11d) indicates that the graupel aloft had descended to below 7.5 km and extended toward the ground. The location of the bottom of graupel area inferred by the algorithm described in this paper is close to where the microburst occurred, as
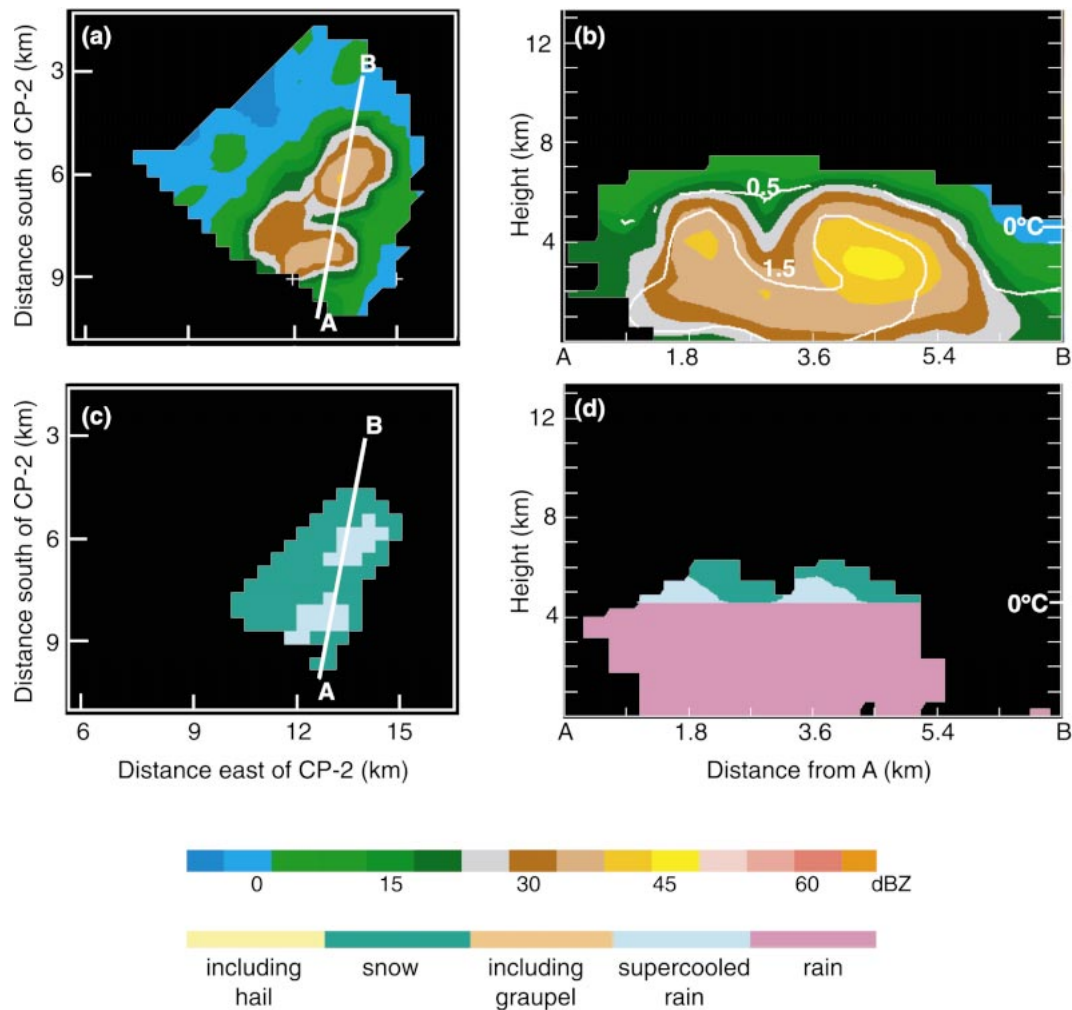
FIG. 7. Horizontal and vertical cross sections of reflectivity, differential reflectivity, and hydrometeor type at 1400 CDT 20 Jul 1986. (a) Horizontal reflectivity at 5-km altitude. (b) Vertical cross section of reflectivity along the line AB shown in (a) with contours of ZDR superimposed. (c) Horizontal cross section of hydrometeor types at 4.5-km altitude. (d) Vertical cross section of hydrometeor type along line AB.

indicated by the center of downdraft (Fig. 11d) and divergent radial velocity (not shown).

b. Volumetric analysis

To get a more general picture of the evolution of the presence of supercooled rain, graupel, and hail in the three-dimensional volume of the storm, time–height frequency distributions were constructed (Fig. 12). The ratio of the number of pixels with a given hydrometeor type to the total number of pixels in the radar echo >10 dBZ at a particular level in the interpolated volume is referred to as the normalized frequency of the hydrometeor type. Supercooled rain (Fig. 12a) occurred mainly during the early stage from 1400 to 1412 CDT. The maximum height at which supercooled rain occurred was 7 km ($-15°$C). The initial occurrence of supercooled rain preceded the earliest occurrence of graupel

and hail. The first appearance of hail (Fig. 12c) was at 1406 at 7.5 km. Later at 1412, the hail extended to 10 km high with the maximum volume of hail at 7.5-km altitude. Immediately after the hail reached its maximum vertical extent, the hail region collapsed dramatically, as evidenced by its steep slope in the time–height plot. By 1418, most of the hail had fallen out of the region above the 0°C level, forming a local maximum in concentration at 3.5-km altitude. It is likely that by 1418 CDT, the hail production was completed and the hail already present was falling out.

Volumetrically within the storm there was more graupel than hail. Graupel (Fig. 12b) first occurred at the same time as the first occurrence of hail but persisted longer. The maximum-sized graupel region was suspended at 7-km altitude at 1418, then descended rapidly, appearing below the 0°C level at 1412. Graupel existed above the 0°C level slightly longer than hail, consistent
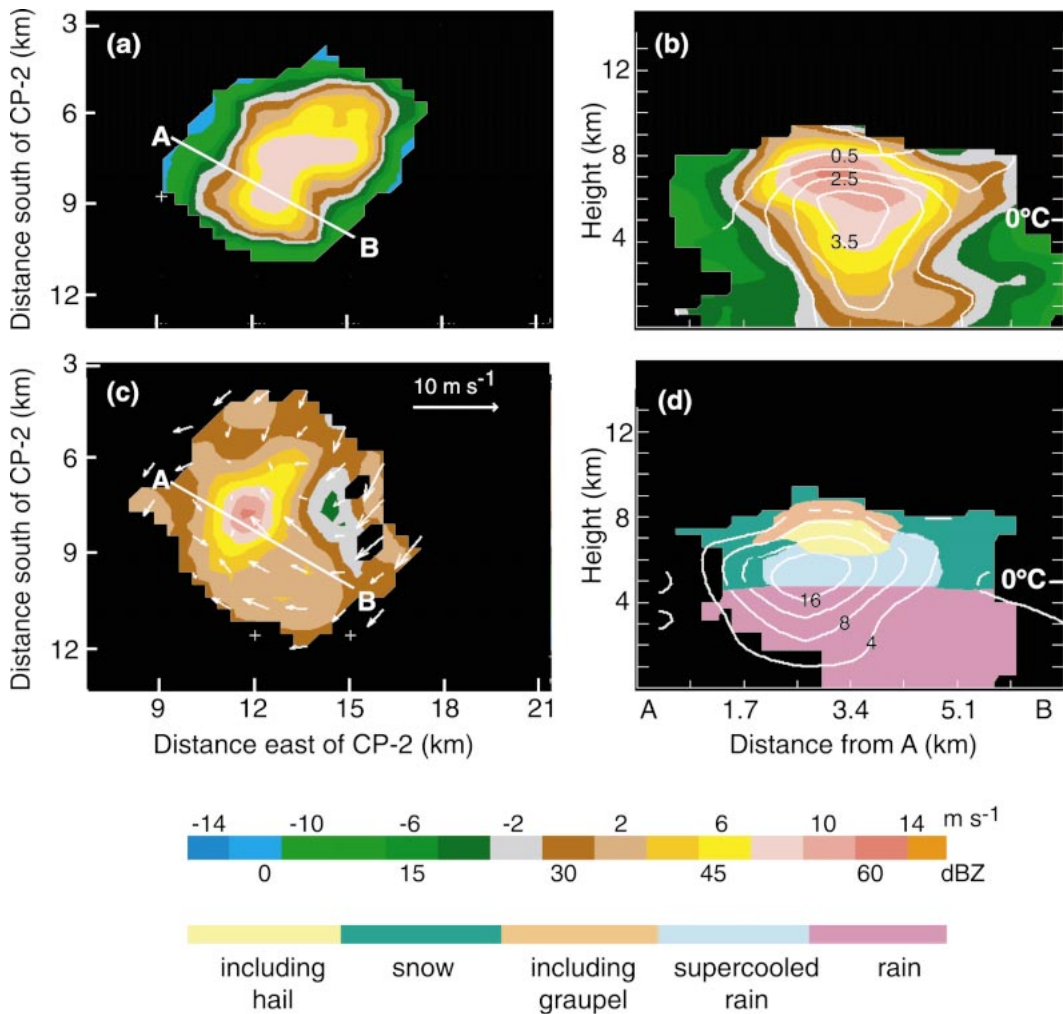
FIG. 8. Horizontal and vertical cross sections of reflectivity, differential reflectivity, synthesized Doppler wind, and hydrometeor type at 1406 CDT 20 Jul 1986. (a) Horizontal cross section of reflectivity at 5-km altitude. (b) Vertical cross section of reflectivity along line AB shown in (a) with contours of ZDR superimposed at 0.5-dB intervals. (c) Horizontal cross section of vertical velocity at 3-km altitude overlaid with horizontal wind vectors. (d) Vertical cross section of hydrometeor type along line AB shown in (c) with contours of vertical velocity at interval of 4 m s^{-1}.

with the lower fall speed of graupel. However the timing of the steep slope in graupel occurrence at 1424 rather than 1418 as was seen for hail indicates that graupel continued to be suspended aloft and possibly produced after hail production had ceased. At later stages, graupel is only found below the 0°C level and the altitude distribution of its occurrence became shallower with time, consistent with the production of smaller solid particles produced later in the storm that survived shorter distances before melting into raindrops. The height distribution of graupel shown in Fig. 12b has several general similarities to Tuttle et al.'s (1989, their Fig. 11) two-dimensional model output. It is difficult to make an exact comparison between a two-dimensional model and three-dimensional observations and as mentioned previously, the mapping between detection of graupel by

the polarimetric radar and its mixing ratio is currently unverified. For example, Tuttle et al.'s plot indicates maximum graupel–hail mixing ratios at 6-km altitude, compared to the Fig. 12b altitude of the maximum frequency of the "including graupel" type at 8-km altitude.

The appearance of supercooled rain in the volume prior to the occurrence of graupel and hail is consistent with an early coalescence process, as concluded by Goodman et al. (1988) and Tuttle et al. (1989). The subsequent occurrence of the mixture of supercooled rain, graupel, and hail above the 0°C level is consistent with their conclusion that the freezing and accretion of supercooled water were responsible for graupel and hail growth. The consistency of microphysical interpretation among the analysis of Goodman et al. (1988) and Tuttle et al. (1989), the hydrometeor-type algorithm used here,
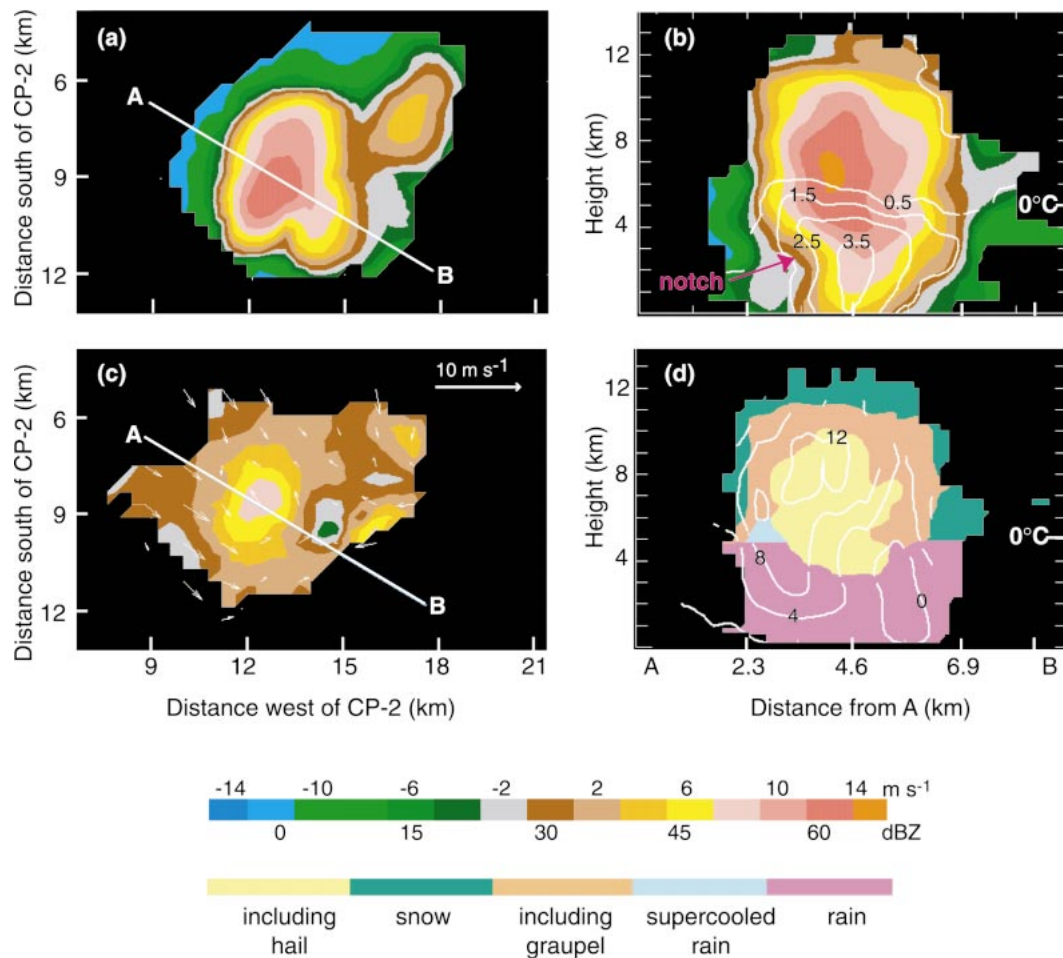
FIG. 9. As in Fig. 8 except at 1412 CDT 20 Jul 1986.

and the 3D dual-Doppler wind field is evidence that the hydrometeor-type algorithm yields physically reasonable results.

The timing and height distribution of supercooled rain, graupel, and hail in the time–height plots can be compared to the microphysical and dynamical evolution of the three-dimensional storm volume inferred from contour frequency by altitude diagrams (CFADs; Yuter and Houze 1995b) of reflectivity and vertical velocity. Figure 13 shows the time sequence of CFADs for reflectivity and vertical velocity corresponding to the time of the cross sections in Figs. 8–11. A key feature of the reflectivity CFAD is the onset of the diagonalization of the mode of the joint frequency distribution of reflectivity and height (Yuter and Houze 1995b). While the distribution of reflectivity above the 0°C level is wide and multimodal at 1406 and 1412, at 1418 the mode of the distribution begins to show signs of diagonalization indicating increasing Z with decreasing height from the top of the echo to 8 km. The beginning of the diagonalization at 1418 CDT is coincident with the fallout of the maximum in normalized frequency of graupel and hail (Fig. 12). By 1424 (Fig. 13g) the storm exhibits a

strong reflectivity distribution diagonalization pattern including a local maximum at the 0°C level characteristic of dominant stratiform microphysical processes. The dominance of stratiform microphysical processes occurred after the fallout of graupel and hail was nearly complete (Fig. 12). Also of note at 1406 and 1412 (Figs. 13a,c) is that while a small portion of the volume is occupied by high reflectivities, the mode of the reflectivity distribution below 0°C level is less than 20 dBZ. This weak echo mode is usually associated with weak echo produced by boundary layer convergence and represents the reflectivities at the base of the updraft during its early stages (Yuter and Houze 1995b).

The CFADs of vertical velocity yield information on the kinematic evolution of the storm volume. At 1406, the mode in the frequency distribution of vertical velocity is <4 m s^{-1} for the depth of the volume. The higher w values associated with the updraft shown in Fig. 8d and the associated supercooled rain, hail, and graupel represent only a small fraction of the volume. At 1412, the main updraft is visible in the CFAD as an outlier in the frequency distribution. The updraft magnitude increases with increasing height consistent with
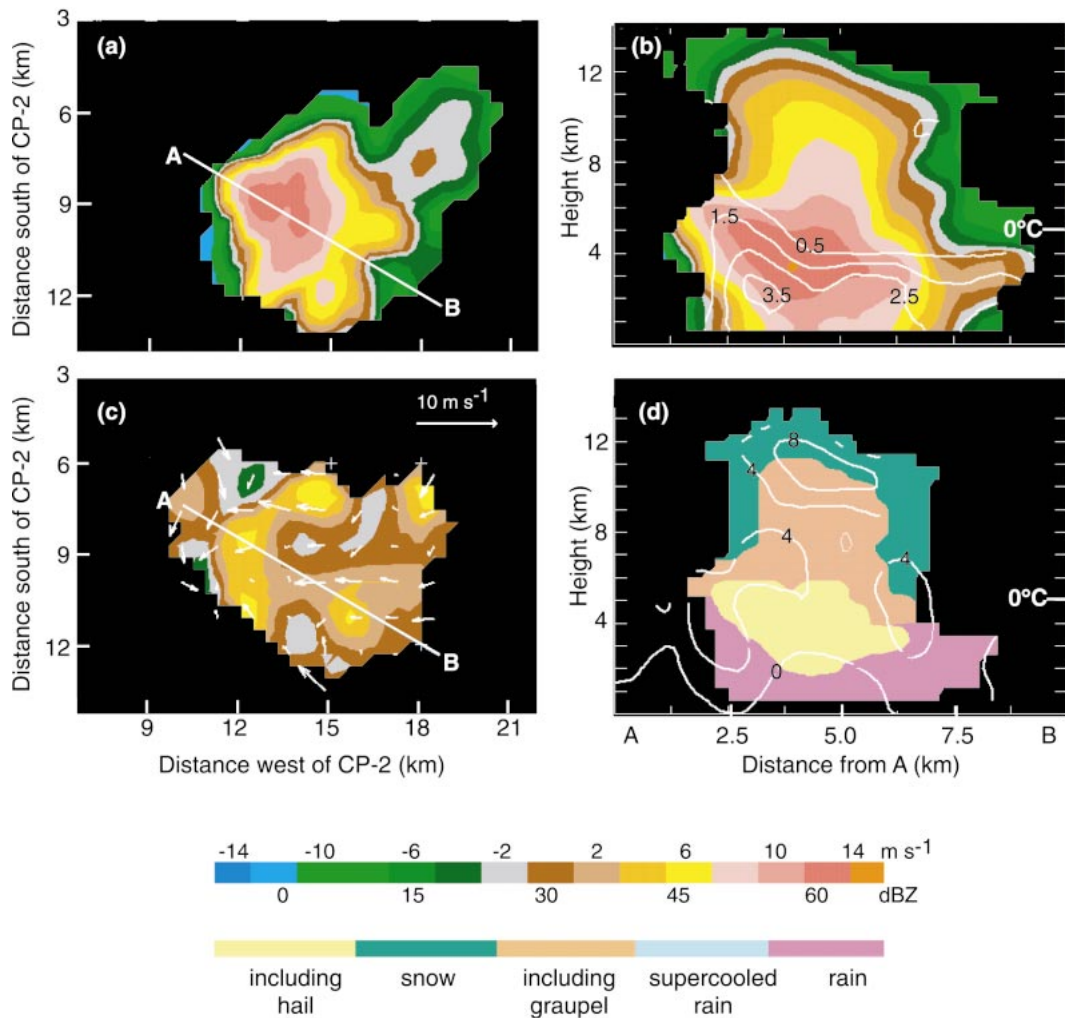
FIG. 10. As in Fig. 8 except at 1418 CDT 20 Jul 1986.

thermodynamic laws. At 1418, when the hail shown in Fig. 10d has begun to descend, the vertical velocities exhibit a larger volume of downdrafts with a peak outlier downdraft at 2.5-km altitude. The magnitude of the outlier updraft has also decreased compared to 1412 and the mode of the distribution is more organized with a weaker associated velocity. By 1424, the strong updraft has disappeared and the volume is dominated by weak updraft velocities <3 m s^{-1} and downdrafts through the depth of the storm.

Dominant accretional microphysical processes are indicated by a lack of diagonalization in the reflectivity CFAD. The timing of the demise of the dominant accretional growth is closely coordinated with the weakening of the main updraft in this single-cell storm, as seen in the weakening of the outliers of the w distribution (right side of Fig. 13). At 1424 CDT, when the reflectivity diagonalization indicates dominant stratiform microphysical processes, the hail has already fallen out but some graupel remains at low levels and the updrafts are weak. Analysis of the volumetric statistics

in the time–height plots of hydrometeor type and the CFADs indicates the prevalence of graupel over hail more clearly than the small sample represented by the cross sections. Although the initial hail embryos are most likely frozen raindrops, growth by riming at upper levels of the storm is a more physically consistent explanation for the presence of graupel at 11 km at 1418 when supercooled water is no longer present.

The high time resolution of the 20 July 1986 MIST data shows that while the updraft velocities are strongest at the top of the storm, the demise of dominant accretional growth as indicated by the diagonalization of the frequency distribution of reflectivity moved from the top of the storm downward. An important factor in accretional growth is the liquid water content that is constrained by temperature for a given vertical velocity. These results indicate that initially accretional growth (coalescence at lower levels and riming at upper levels) dominates through the depth of the convective cell. As the storm evolves, despite the larger vertical velocities available within the upper portions of updrafts to both
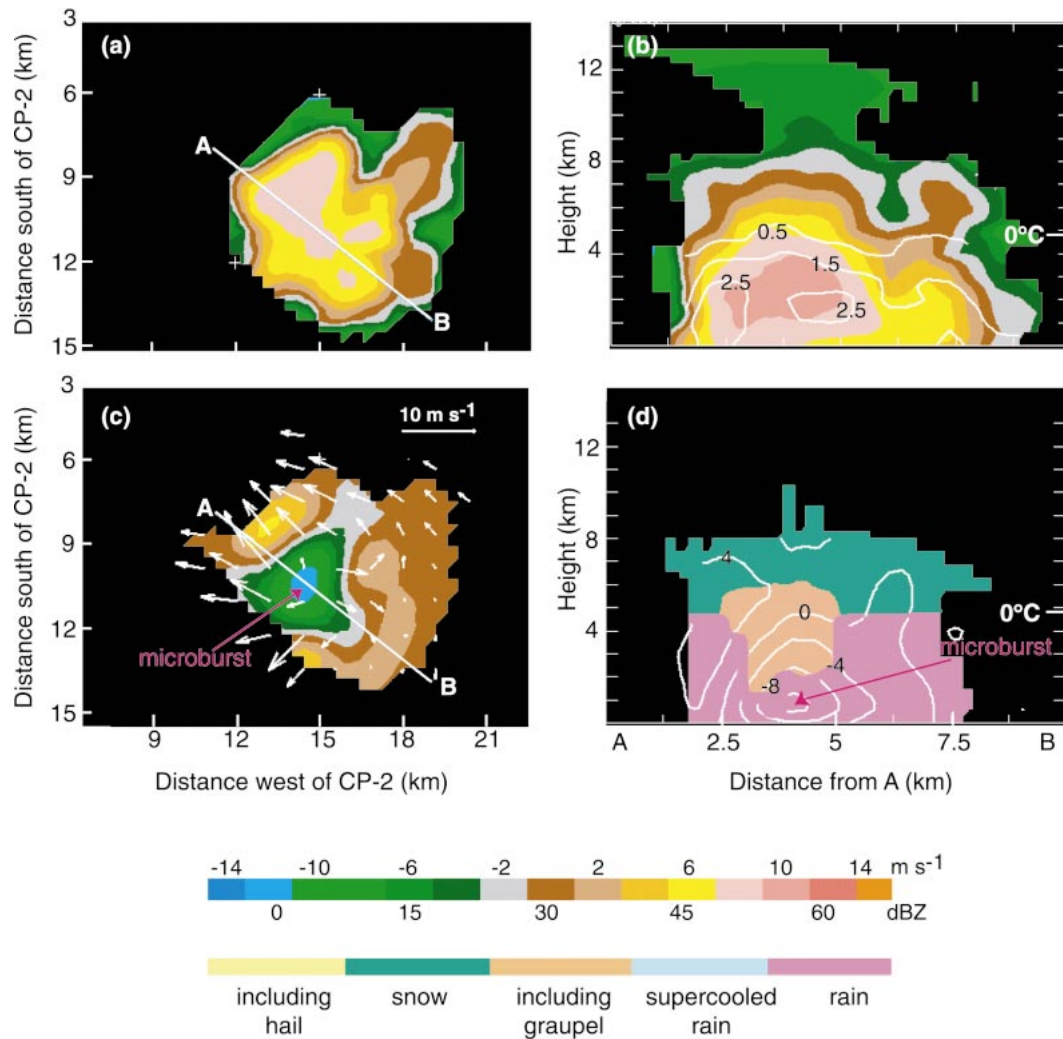
FIG. 11. As in Fig. 8 except at 1424 CDT 20 Jul 1986 and the horizontal cross sections of reflectivity in (a) and synthesized wind in (c) are at 0.5-km altitude.

keep larger particles aloft and support condensation of liquid water, the lower temperature at the top of the echo acts as an apparent brake on the condensation process. Accretional growth slows as cloud liquid water at the top of the storm is depleted. The reduction in cloud water at the top of the storm leads to the demise of accretional growth processes and the increasing dominance of slower vapor depositional growth processes from the top of the storm downward. Examination of Fig. 19 in Kingsmill and Wakimoto (1991) corroborates this interpretation; the ragged cloud top at 1424 CDT[4] is evidence of a depletion of cloud liquid water. A related inference is that most of the accretional growth would occur at midlevels where updraft velocity and

temperature are at an optimum balance. The exact nature of this balance would best be determined by cloud modeling studies that are beyond the scope of this work.

The analysis of the evolution of hail development in the 20 July 1986 single-cell case presented in this paper is confirmatory of previous work on these same data. Although similar volumetric data of hydrometeor type are not available in the previous studies, the confirmation of the sequence of steps in the microphysical development of hail acts to indirectly validate the simple hydrometeor classification algorithm utilized in this study. By presenting the data in terms of the time variation of the vertical distribution of objectively derived hydrometeor type (Fig. 12) and CFADs (Fig. 13), we have been able to examine the evolution of particle types and kinematics within the entire storm echo volume. The CFADs provide a bridge to the Yuter and Houze (1995b) CFADs and aid in interpreting the particle fountain conceptual model. The plot of the time variation of

[4] Kingsmill and Wakimoto used central standard time rather than central daylight time as their time base. Their Fig. 19 refers to the storm volumes starting at 1318 and 1324 CST, which correspond to our volumes at 1418 and 1424 CDT.
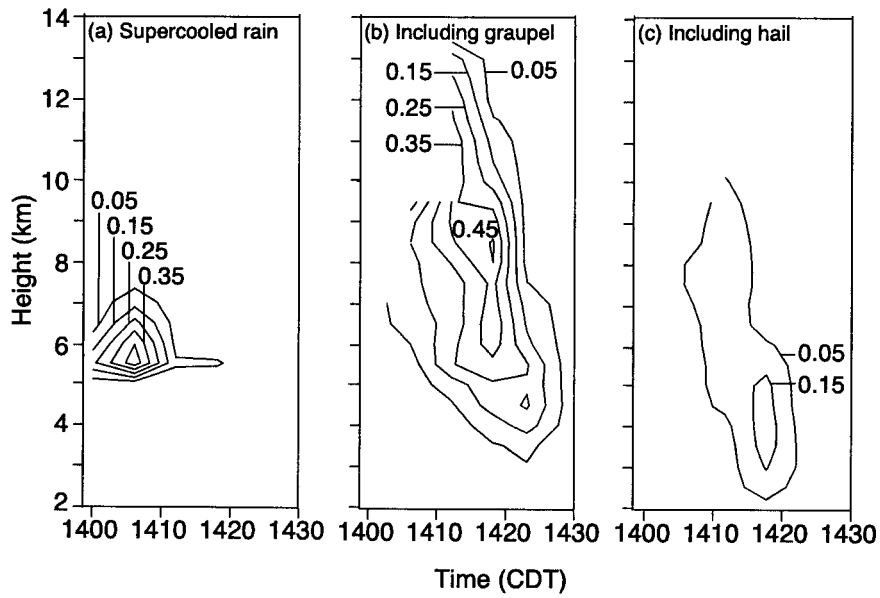
FIG. 12. Time variation of the vertical distribution of normalized frequency of hydrometeor
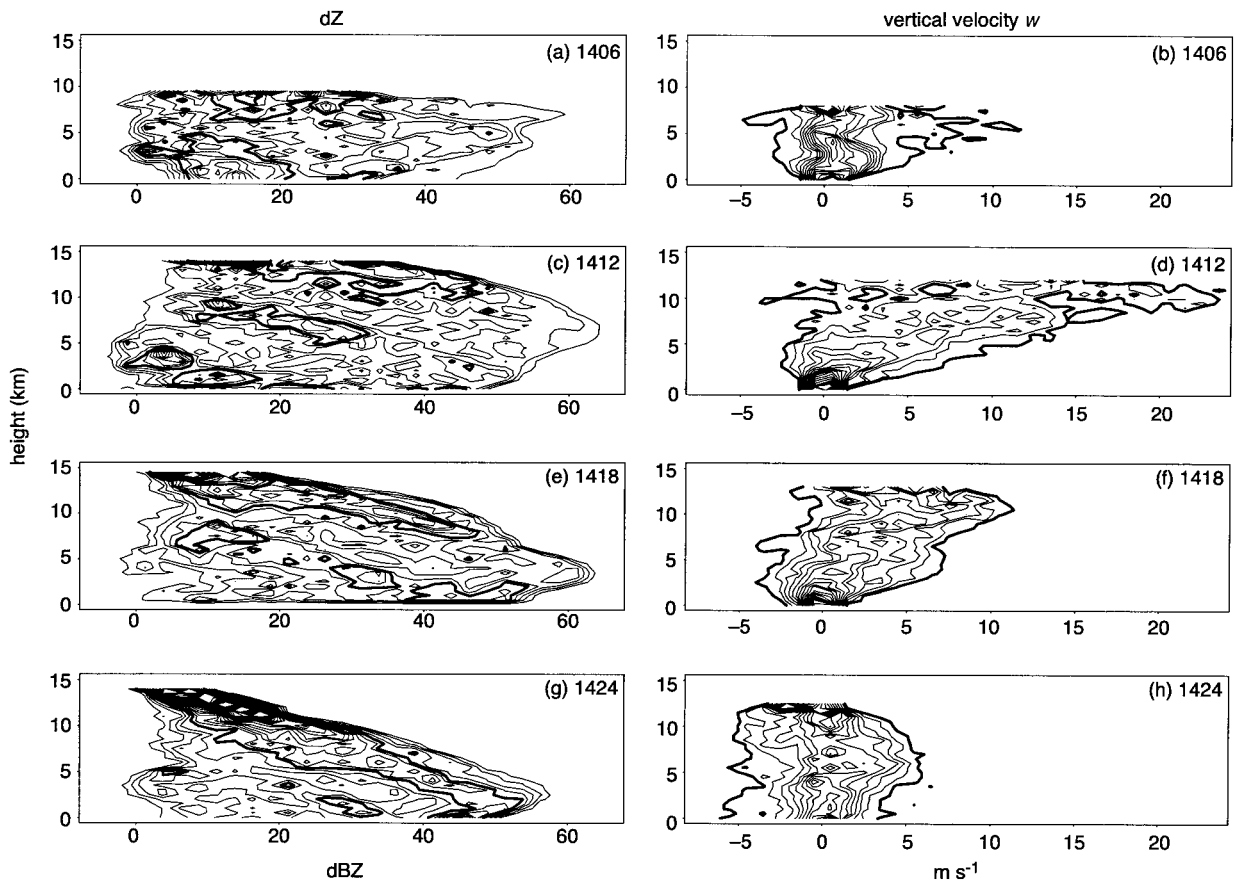type for supercooled rain, graupel, and hail.

FIG. 13. Time series of CFADs of (left) radar reflectivity and (right) vertical velocity. For reflectivity CFADs the bin size is 2.5 dBZ and the plot is contoured at intervals of 2% data dBZ^{-1} km^{-1} with the 5% dBZ^{-1} km^{-1} contour highlighted. In the vertical velocity CFADs the bin size is 1 m s^{-1}, and the plot is contoured at intervals of 2% of data m^{-1} s km^{-1} with the 30% m^{-1} s km^{-1} contour highlighted.
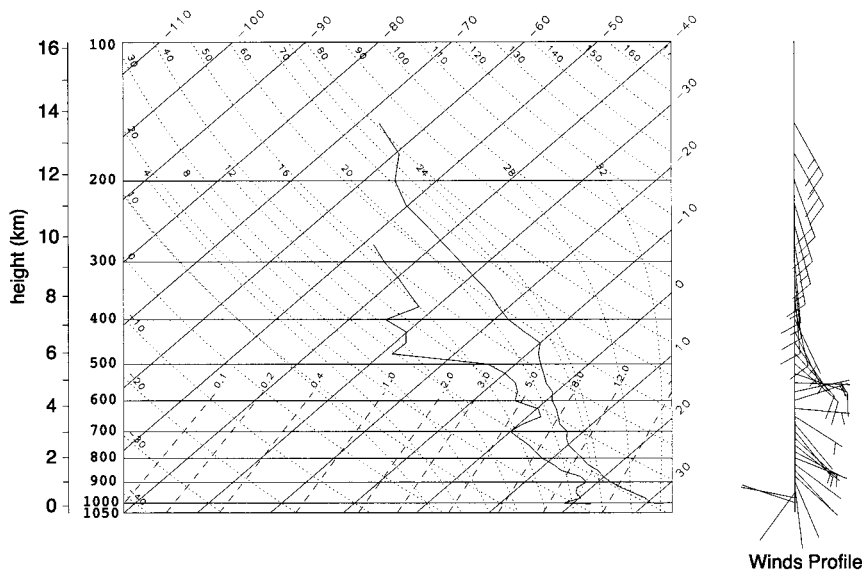
FIG. 14. Environmental sounding taken from Redstone, AL, at 1300 CDT 6 Jul 1986. Solid lines show temperature and dewpoint. Dashed lines are saturation mixing ratio. Dotted curves are the dry and moist adiabats. Wind barbs are at 25-hPa intervals. Full barb is 10 m s^{-1}.

the vertical distribution of objectively derived hydrometeor type allows us to synthesize in one plot the hydrometeor inferences derived in previous work on the 20 July 1986 case based on cross sections and time–height profiles of the observed radar variables (i.e., Z, ZDR, and LDR). This type of synthesis plot aids in simplifying comparison of this cell to other cells in other storms. In the next section, we will examine a hail-producing cell within a multicellular storm to address the generality of the results from the well-studied single-cell 20 July 1986 case.

5. Hail-producing cell within a multicellular storm on 6 July 1986

The MIST case from 6 July 1986 provides an additional example of a rapidly growing and intensifying cell in a low-shear environment. The thermodynamic environment of this case was typical of a warm-base airmass storm and is similar to the 20 July case. The 1300 CDT Redstone, Alabama, sounding (Fig. 14) indicated conditional instability below 900 mb. The temperature lapse rate was equal to or slightly greater than the dry-adiabatic lapse rate. Any small disturbance would have easily triggered convection. The surface mixing ratio was 16.6 g kg^{-1}. Above the surface, a deep moist layer extended up to 500 mb. The 0°C level in the environment was at 4.5-km altitude. An undiluted parcel ascent from the surface would yield a cloud base at 862 mb (~1.5 km MSL), a cloud-base temperature of 19°C, and a 0°C level in the updraft of 5.5 km. Adiabatic liquid water at 500 mb following the ascent of this undiluted parcel was 8.6 g kg^{-1} or 5.5 g m^{-3}. The CAPE was 2651 J kg^{-1}. The 0°C level in the updraft

was 4 km higher than the cloud base, which allowed a considerable vertical distance through which the coalescence process could operate.

a. Cross-section analysis

At 1500 CDT, the convection started to occur south-southeast of the CP-2 radar in the form of numerous isolated small cells and propagated generally westward and northwestward. The propagation of the convection was discrete rather than continuous. New cells tended to originate some distance ahead of the decaying cells. A gust front was evident ahead of the convection after 1623 CDT, and from that time on, the gust fronts moved rapidly away from the convection, cutting off the supply of low-level inflow. The convection died soon after. We focus on a single convective cell, 60 km southeast of the CP-2 radar, from its initial to mature stage. A sequence of horizontal cross sections of reflectivity at 4.5-km altitude illustrate the life cycle of a particular cell located near $x = 24$ km and $y = 23$ km (Fig. 15). The vertical cross sections for each time corresponding to the line AB are shown in Fig. 16.

At 1518 CDT, echo ~10 dBZ occurred between 3- and 4-km altitude (not shown), associated with a new cell at $x = 24$ km and $y = 23$ km located near a vigorous cell at $x = 30$ km and $y = 23$ km. Six minutes later (1524 CDT; Figs. 15a and 16a), the new cell developed a maximum reflectivity of 58 dBZ centered at 5-km altitude. The 50-dBZ contour encompassed an area of 1.5 km in diameter. The 30-dBZ reflectivity contour extended from 3- to 7-km altitude (Fig. 16a) and was about 5 km wide (Fig. 15a). The gradient of reflectivity around the cell was very large, decreasing outward from
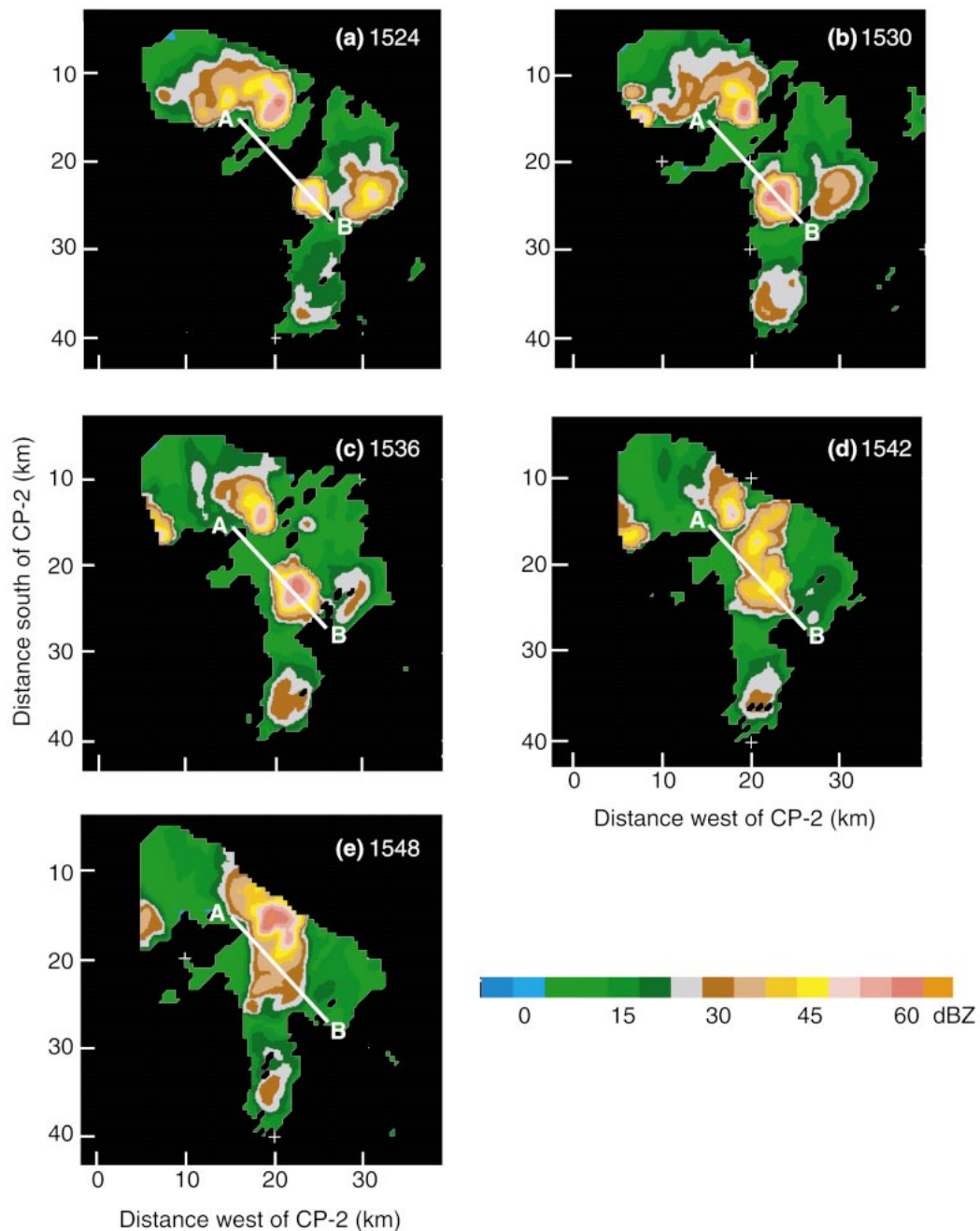
FIG. 15. Time series of horizontal cross sections of reflectivity at 4.5-km altitude. Line AB indicates the location of vertical cross sections in Fig. 16. Grid origin ($x = 0$, $y = 0$) is at the CP-2 radar. Time is in CDT.

the center of the cell by 30 dBZ within 2 km. Surface reflectivity at this time was only 15 dBZ, indicating light rain $<\sim 0.5$ mm h^{-1} at the surface.

Since interpolation smoothes some features, we checked the raw data (not shown) from 1512 to 1524 CDT to confirm that the cell was indeed suspended and did not touch the ground. At 1518:39 CDT, a 2 km $\times$ 2 km region with a reflectivity of about 10 dBZ emerged next to a cell at 35-km range and azimuth 135° in the

7.2° and 8.4° elevation angle scans (about 4–5 km high). No detectable echo was present in other elevation angles at this range. The accompanying ZDR to this suspended echo was close to zero. Detectable precipitation began to form between 4- and 5-km altitude at 1518. At 1524: 42, an area of about 4 km $\times$ 4 km was present with the reflectivity of 58 dBZ in the 8.4° elevation angle.

Within 6 min, the cell reflectivity increased from 10 to 58 dBZ. Evidently large particles quickly formed in
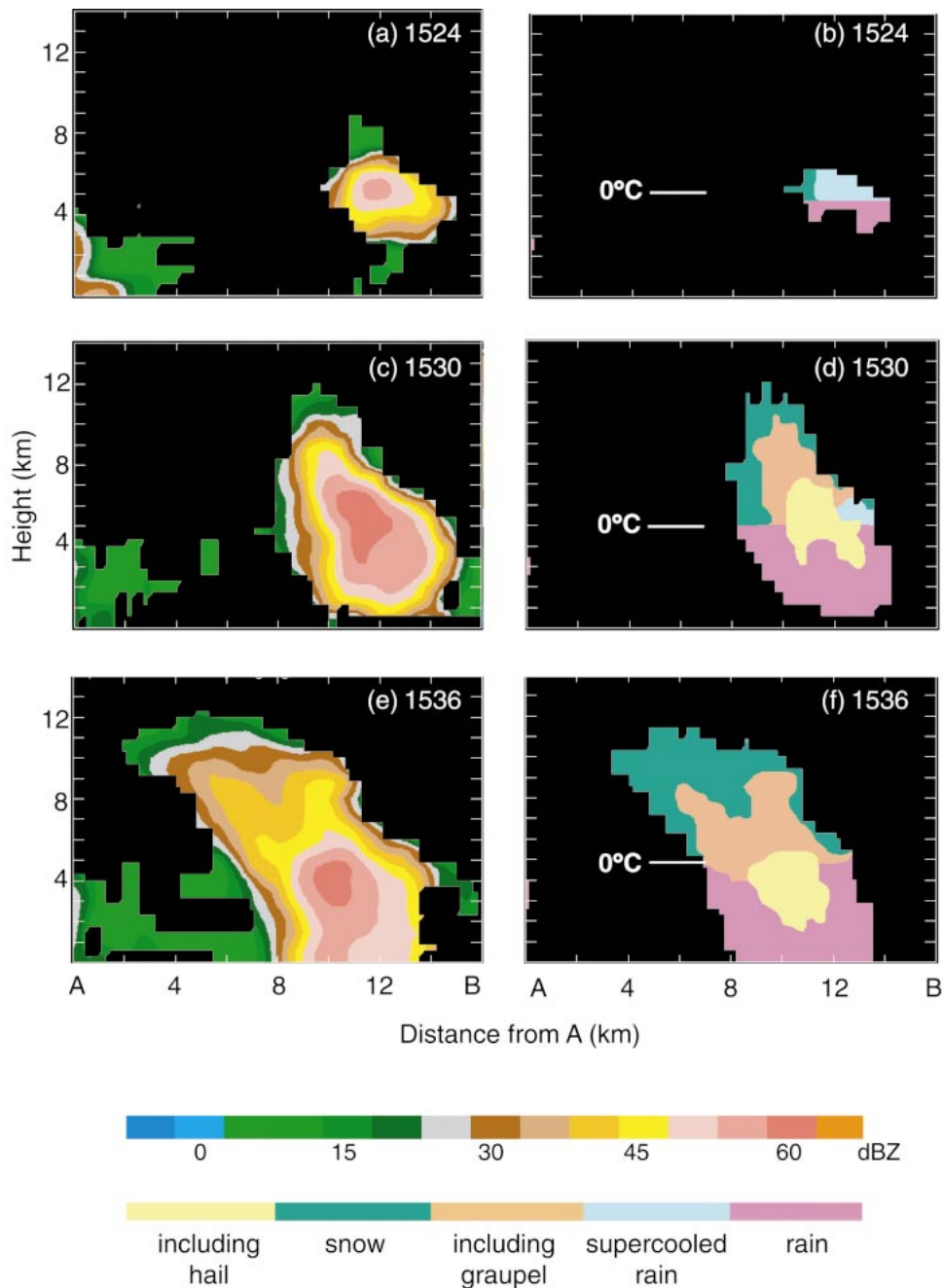
FIG. 16. Vertical cross sections of (left column) reflectivity and (right column) hydrometeor types taken along line AB shown in Fig. 15. Time is in CDT.

the storm core at 3–4 km above the lifting condensation level (LCL). The hydrometeor-type algorithm indicates supercooled rain inside the reflectivity core (Fig. 16b). Liquid water both below and above the 0°C level and no graupel/hail in the cell strongly suggest a dominant coalescence process in the initial development of the cell. ZDR within the region of >50 dBZ had a maximum 4.5 dB (not shown) corresponding to raindrops with

median mass-weighted diameter of ∼3 mm (Bringi and Chandrasekar 2000).

Rapid growth continued over the next 6 min (Figs. 16c,d). At 1530 CDT, the 5-dBZ echo top rose from 8 to 12 km (Fig. 16c), a rising rate of 11 m s^{-1}. The ratio of maximum interior vertical motion to cloud-top rise rate is assumed to be somewhere around 1.5 and 2.3 (Woodward 1959; Kingsmill and Wakimoto 1991;
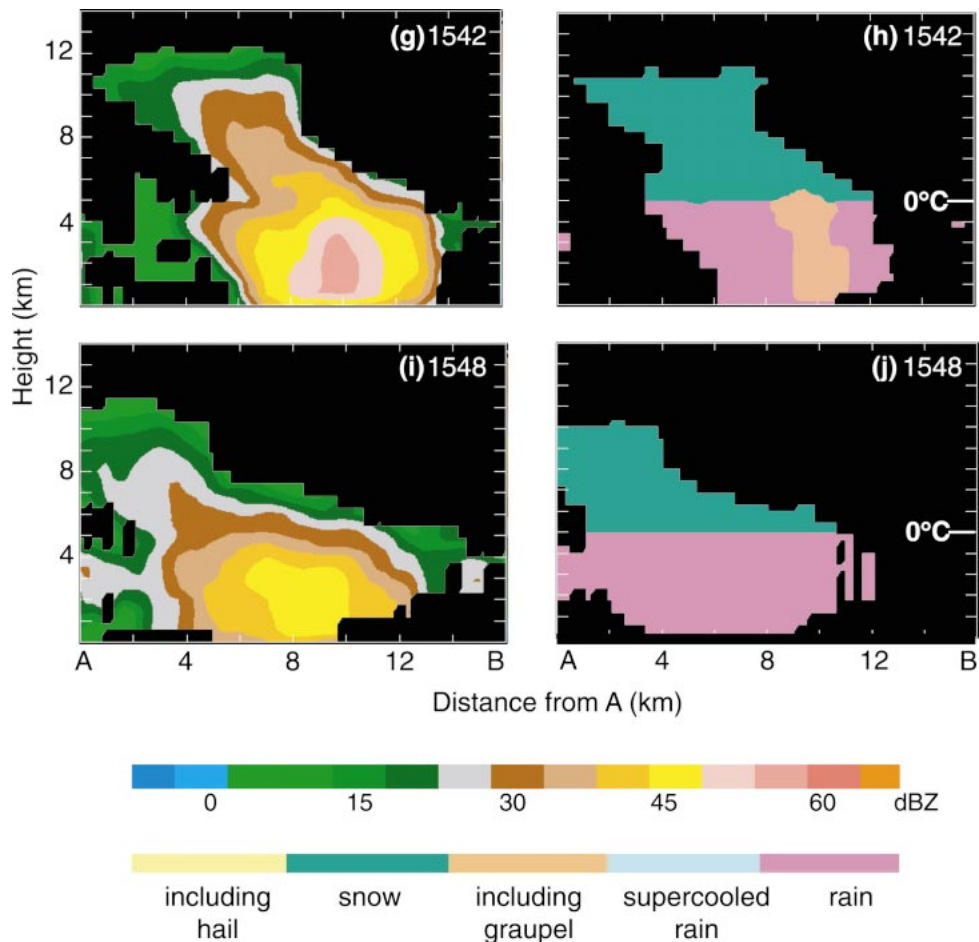
FIG. 16. *(Continued)*

Keenan et al. 1994); this would suggest the maximum vertical velocity to be 16–25 m s^{-1}. The maximum reflectivity was 66 dBZ at 6 km. The 50-dBZ contour bounded an area 5 km wide and 7.5 km high (extending from 1.5 km above surface to 9 km). The suspended reflectivity was still present (Fig. 16c) but was about to collapse toward the surface. The gradient of reflectivity was large both near the surface and at the top of the echo, suggesting rapid upward motion of echo top due to a strong updraft and rapid sinking of heavy particles toward the surface. The cell is slightly tilted toward the northwest in connection with a southeasterly shear. The inferred hydrometeor type indicates that hail was present in the reflectivity core of the storm from 3- to 7.5-km altitude (Fig. 16d). The bottom of the hail region was already below 0°C level, indicating that a portion of the hail was descending. A graupel region extended from 0°C level to 8.5 km. Only a small area of supercooled water remained on the upwind side (right side of Fig. 16d); this is probably a result of less ice nuclei in the fresh updraft on the upwind side (Hobbs and Rangno 1985). The abundance of graupel and hail within the cell at 1530 versus no graupel and hail 6 min earlier at

1524 indicates a fast glaciation and hail formation process similar to the July 20 case. The dramatic rise of the echo top likely associated with latent heat from the glaciation process was again present in this case.

By 1536 CDT, 18 min after the appearance of the initial 10 dBZ, the strength of the reflectivity core has decreased slightly from 66 to 60 dBZ (Fig. 16e). The previously suspended reflectivity core had completely broken toward the surface, with heavy rain of 54 dBZ reaching the ground. The top of the cell developed laterally and was at a similar height as at 1530 CDT. Hydrometeor-type information (Fig. 16f) shows that hail had fallen completely below the 0°C level. The graupel region remained above the hail region, with its top edge at 9-km altitude. The increasing distance between the top of the graupel region and the top of the hail region is attributed to the greater fall velocity of hail, which led to its rapid descent despite an active updraft in the upper levels.

By 1542 CDT, the upper part of the cell began to collapse. The higher reflectivity regions (Fig. 16g) associated with the larger particles descended much faster than lower reflectivity regions. The 45-dBZ contour de-
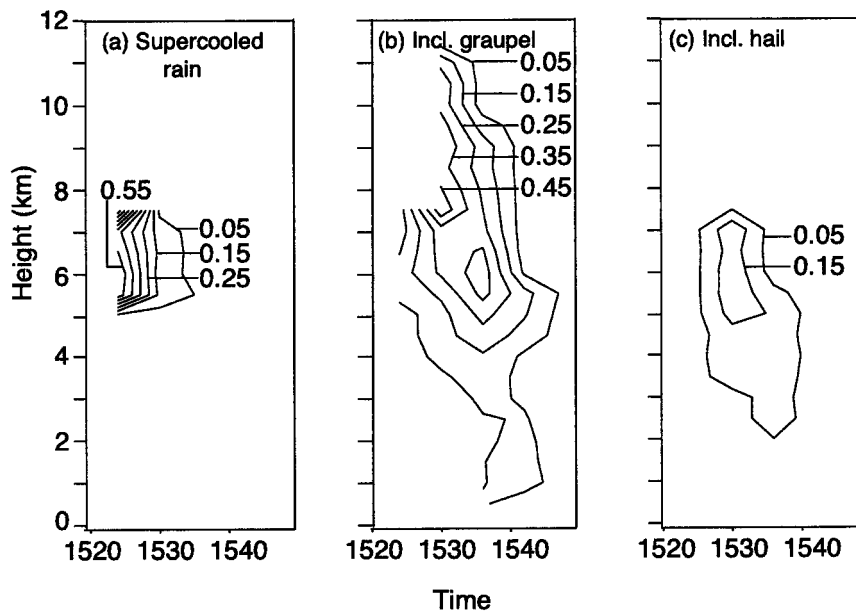
FIG. 17. As in Fig. 12 but for the 6 Jul 1986 storm.

scended 4 km in 6 min, and the 35-dBZ contour descended 1 km in the same time period. The echo top represented by the 14-dBZ contour remained close to 12-km altitude. The ZDR field was close to zero above 4 km (not shown), a characteristic feature of a mature or decaying cell. The hydrometeor classification algorithm (Fig. 16h) indicates no hail at this time above the 0°C level. The graupel region decreased dramatically in altitude from its position at 1536. At 1548 (Figs. 16i,j), the cell was continuing to weaken and decay. No graupel was left above or below the 0°C level. The weakened cell gradually moved north and merged with other cells, losing its identity (Fig. 15e).

Similar to the 20 July case, the 6 July cell grew and decayed rapidly. Within 6 min, the cell grew from barely detectable to having 58-dBZ reflectivity in its core. In the early stage of the cell, large raindrops, possibly in small concentrations, were produced by coalescence and carried above the 0°C level. The coexistence of liquid water and frozen drops provided an ideal condition for fast accretion to produce hail. The decay process was very fast. Eighteen minutes after the "first echo," the region of 54-dBZ reflectivity had reached the ground. The reflectivity maxima remained suspended for about 12 min. No stratiform precipitation formed after the intensive convective precipitation. The cell simply collapsed. After the heavy particles fell out, small ice crystals were dispersed and evaporated. No significant growth of aggregates was evident.

b. Volumetric analysis

Time–height distributions of diagnosed hydrometeor type are shown in Fig. 17. They are similar to the July

20 case. Supercooled rain occurred only in the early stage of the storm from 1518 to 1530. The depth of supercooled rain was 2.5 km, with the top at 7.5 km (−20°C). The occurrence of supercooled rain occurred prior to the onset of graupel and hail. Hail first appeared at 1524, 6 min after the first appearance of supercooled rain. Hail extended up to 8-km altitude briefly. The maximum size of the hail region in the cell occurred at 1530 at 6–7-km altitude. After 1530, the hail quickly fell out of the upper levels. The hailstones descended as far as 3 km below the melting level before melting sufficiently to be no longer identifiable as hail. The whole process of hail formation, descent, and melting occurred over 15 min. Graupel above the 0°C level was present from 1524 to 1542, with the maximum at 1530 at 6 km. Graupel extended to 12-km altitude at 1530, much higher than supercooled rain and hail. The depth of the layer of graupel decreased with time. Graupel extended to the ground at 1536.

Similar to the 20 July 1986 case, the supercooled rain in the early stage of cell evolution and the appearance of the hail and the mixture of water and graupel 6 min after supercooled rain first appeared clearly show that rain is first carried above the 0°C level and becomes supercooled rain. Coalescence growth of initial raindrops and later freezing of drops and accretion growth of graupel/hail are suggested to be the primary precipitation process in this rapidly growing cell. The similarity of the microphysical evolution during the development of hail of the 20 July 1986 single-cell storm and the cell within the multicellular storm on 6 July 1986 has ruled out that the mechanisms of hail development in the 20 July 1986 storm represented a special case unique to single-cell storms. Although not defin-
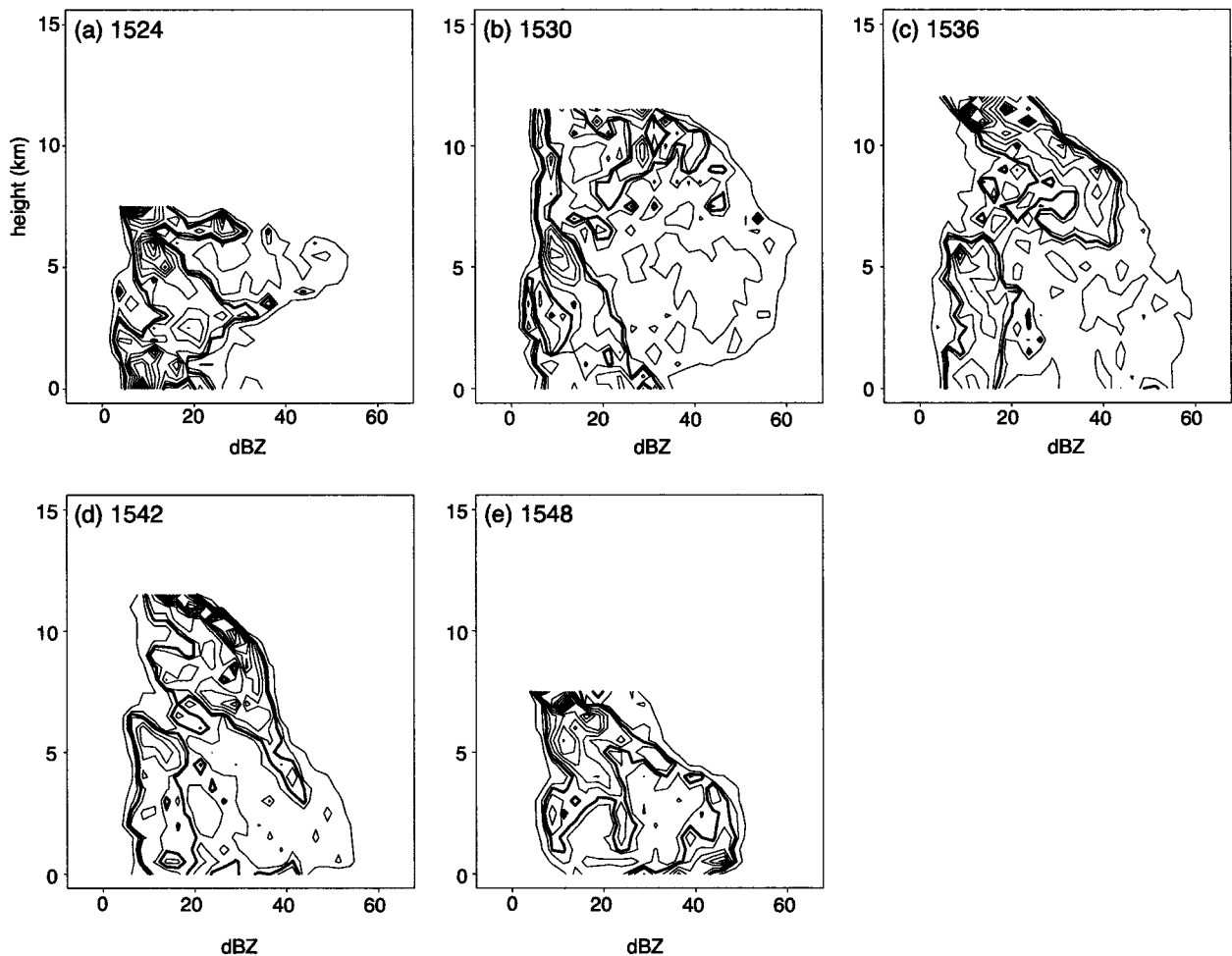
FIG. 18. Time series of CFADs of radar reflectivity for the 6 July 1986 storm. The reflectivity CFAD bin size is 2.5 dBZ and the plot is contoured at intervals of 2% data per dBZ per km with the 5% dBZ^{-1} km^{-1} contour highlighted. Time is in CDT.

itive, these results indicate that the physical processes associated with hail development are likely generally similar throughout storms in Alabama. The differences in the CFADs for the 20 July 1986 and 6 July 1986 cases after the hail has fallen out indicate differences in the microphysics within decaying isolated single cells and cells within multicellular storms.

Examination of joint probability distribution of reflectivity and height (Fig. 18) centered on the cell examined in the cross sections shows that the distribution of reflectivity was wide at all levels and multimodal at several levels. Until 1542 CDT, the mode of reflectivity at lower levels is <20 dBZ, associated with weak radar echos produced by convergence in the boundary layer (Yuter and Houze 1995b). At 1548 CDT, the low-level reflectivity mode is >30 dBZ, indicating convergence has weakened and that fallout of heavier particles from the cell has become the dominant process at low levels. Hail and graupel represented only a small fraction of the volume. At 1536, the peak in hail and graupel development, reflectivities >40 dBZ constituted less than

20% of the cell's echo volume. Unlike 20 July 1986, while trends toward diagonalization in the reflectivity mode are present in the CFADs for 1536, 1542, and 1548, the distribution remains multimodal and clear diagonalization of the reflectivity distribution is not expressed. One can infer that accretion continued as the dominant microphysical process until 1548. We were unable to examine this cell as a separate entity within the multicellular storm past 1548 CDT as a new cell to the north spread into the area where this cell was previously located (Fig. 15). Without vertical velocity data it is not possible to examine the frequency distribution of updrafts and downdrafts and the timing of their evolution relative to the microphysical evolution.

6. Conclusions

Two rapidly growing, hail-producing storms from the MIST project in 1986 were analyzed to examine the details of the microphysical evolution. Both cases were examples of extremely efficient accretional growth pro-

cesses and produced hail within 10 min. A simple hydrometeor classification algorithm was used (section 3) tailored to the strengths and weaknesses of the MIST multiparameter radar dataset (S-band Z and ZDR, and X-band LDR) obtained by the NCAR CP-2. Application of the hydrometeor classification algorithm to the radar data allows us to augment previous work by permitting a consistent physical interpretation of the multiparameter fields and applying this interpretation to the entire storm volume as well as to selected cross sections.

The first case, an isolated cell from 20 July 1986, has been the subject of several previous studies (Wakimoto and Bringi 1988; Goodman et al. 1988; Tuttle et al. 1989; Kingsmill and Wakimoto 1991). We concur with these previous authors that the hail and graupel embryos were likely raindrops that grew rapidly by coalescence within the updraft and then froze. The confirmatory nature of our analysis based on a simple hydrometeor classification algorithm serves to indirectly validate that methodology. Our analysis adds information on the timing and height distribution of the supercooled rain, graupel, and hail within the bulk storm volume (Fig. 12). Supercooled rain was present only in the early stages of the cell evolution and lasted about 8–12 min. The depth of the supercooled rain layer extended 1–2 km above the 0°C level. Dramatic growth of the echo top and intensification of reflectivity occurred after the onset of glaciation (i.e., ZDR decrease above the 0°C level). This is attributed to the latent heat released when the supercooled raindrops froze (Cotton and Anthes 1989). Hail and graupel occurred several minutes after the first appearance of supercooled rain. The most frequent hail occurrence was concentrated at 6–7-km altitude. Graupel was present at higher altitudes and encompassed more of the storm volume than hail. Despite its smaller size, graupel began to fall out below the 0°C level at the same time as hail (Figs. 12 and 17). Whereas the hail region was more closely centered on the updraft (Figs. 8 and 9), the graupel region capped the hail and extended laterally away from the center of the updraft into regions with weaker vertical velocities. Whether the "including graupel" category used in this study is actually graupel or small hail cannot be answered with the radar data from MIST. Future studies using S-band LDR could be able to distinguish the density of the particles. The X-band LDR from MIST is of insufficient quality to make this subtle distinction.

The negative buoyancy of the rapidly formed heavy precipitation particles led to a quick collapse of the updraft and decay of the cell. As heavy particles represented by graupel and hail (Fig. 9d) started to descend, the drag of the heavy precipitation weakened the updraft below. As a result, from midlevels downward the air quickly becomes negatively buoyant, while the upper levels containing lighter particles are less affected by the load of precipitation and remain positively buoyant (Fig. 10d). The resulting vertical gradient of buoyancy [as shown in Kingsmill and Wakimoto (1991)'s retrieval

of this case in their Fig. 9] can produce a pressure perturbation minimum in the layer between (Houze 1993, p. 223), which is able to initiate inflow into the cell, resulting in a "constriction" feature of the cloud (Fujita and Black 1988; Kingsmill and Wakimoto 1991). The analysis of radial velocity for cases other than 20 July by Kingsmill (1991) also showed maxima in radial convergence that occurred above the reflectivity core just after glaciation. This midlevel inflow is local to the collapsing convective cell and was short lived.

Examination of the joint frequency distribution of reflectivity and vertical velocity with height (Fig. 13) showed that the microphysical and kinematical evolution of this isolated cell was more closely coupled than in the multicellular storm examined by Yuter and Houze (1995b). Diagonalization of the frequency distribution in reflectivity, indicative of the demise of accretion growth as the dominant microphysical process, occurred through the depth of the storm at 1424 CDT after the fallout of the hail and most of the graupel (Fig. 12). Updrafts >5 m s^{-1} were still present but the stronger magnitude drafts >20 m s^{-1} had subsided. The high time resolution of the data also reveals that the diagonalization of the frequency distribution of reflectivity moved topdown in the storm volume. Accretion growth processes apparently weakened first high in the storm, where colder temperatures limited cloud water concentrations and the available cloud water was able to be depleted more quickly than at mid- to lower levels.

The second case examined a single cell within a multicellular storm on 6 July 1986. The microphysical evolution as expressed in the cross sections (Figs. 15 and 16) and time–height analysis of hydrometeor type (Fig. 17) is very similar to the 20 July storm. This similarity indicates the generality of the microphysical sequence leading to the rapid production of hail for the extensively studied 20 July 1986 storm. The distributions of reflectivity with height (Fig. 18) for the portion of the cell lifetime examined did not transition to a single-mode diagonalization pattern. It is not clear whether after 1548 CDT this pattern would have developed since this particular cell lost its identity: a younger neighboring cell was expanding into its location. The similar behavior of the rapidly growing, hail-producing single isolated cell and a cell within a multicellular storm adds further support to Houghton's (1968) hypothesis that single cells within a multicellular storm have nearly independent precipitation processes except for the recycling of particles from one cell to another.

The particle fountain conceptual model describes multicellular storms as ensembles of particle fountains at different stages of their life cycles. The single cells examined in this study permitted examination of the details of the life cycle of single particle fountains. For the isolated cell on 20 July 1996, the timing of the kinematically active portion of the storm with the strongest updrafts coincided with evidence of dominant accretion. The microphysics did not begin to exhibit the

demise of dominant accretional growth until the updrafts had weakened significantly at 1424 CDT. The evolution of the kinematics and microphysics are closely coupled for individual particle fountains (i.e., single cells). The observed tendency of the microphysical evolution of multicellular storms to exhibit dominant stratiform microphysical processes while strong updrafts are still present, seen in the analysis of the Florida multicellular storm in Yuter and Houze (1995b), is a property of the ensemble of particle fountains. As the multicellular storm develops, progressively more older particle fountains are present. Volumetrically these older particle fountains begin to dominate the storm, even while a number of younger particle fountains are still in their active stages.

Evidence from the storms analyzed from MIST suggests that the rapid growth of heavy precipitation may shorten the lifetime of an individual cell compared to cells without hail. The combination of enhancement of the updraft at upper levels of the storm by latent heat released by glaciation and the fallout of heavy precipitation acts to tear the cell apart at midlevels (Kingsmill and Wakimoto 1991). The remnant updraft, no longer connected to the surface, contributes to the weakly buoyant air aloft and an environment favorable for depositional growth. If the cell (particle fountain) was part of a multicellular storm, the production of hail and graupel would act to hasten the time when stratiform precipitation processes became dominant in the storm volume as individual cells (particle fountains) would reach their mature stage more rapidly.

REFERENCES

Aydin, K., T. A. Seliga, and V. Balaji, 1986: Remote sensing of hail with a dual linear polarization radar. *J. Climate Appl. Meteor.,* **25,** 1475–1484.

Bader, M. J., S. A. Clough, and G. P. Cox, 1987: Aircraft and dual-polarization radar observation of hydrometeors in light stratiform precipitation. *Quart. J. Roy. Meteor. Soc.,* **113,** 469–489.

Braham, R. R., 1964: What is the role of ice in summer rain showers? *J. Atmos. Sci.,* **21,** 640–645.

Bringi, V. N., and V. Chandrasekar, 2000: *Polarimetric Doppler Weather Radar.* Cambridge University Press, 500 pp.

——, T. A. Seliga, and W. A. Cooper, 1984: Analysis of aircraft hydrometeor spectra and differential reflectivity (Z_{DR}) radar measurements during the Cooperative Convection Precipitation Experiment. *Radio Sci.,* **19,** 157–167.

——, J. Vivekanandan, and J. D. Tuttle, 1986: Multiparameter radar measurements in Colorado convective storms. Part I: Hail detection studies. *J. Atmos. Sci.,* **43,** 2564–2577.

——, L. Liu, P. C. Kennedy, V. Chandrasekar, and S. A. Rutledge, 1996: Dual multiparameter radar observations of intense convective storms: The 24 June 1992 case study. *Meteor. Atmos. Phys.,* **59,** 3–31.

——, K. Knupp, A. Detwiller, L. Liu, I. J. Caylor, and R. A. Black, 1997: Evolution of a Florida thunderstorm during the Convection and Precipitation/Electrification Experiment: The case of 9 August 1991. *Mon. Wea. Rev.,* **125,** 2131–2160.

Browning, K. A., and Coauthors, 1976: Structure of an evolving hailstorm. Part V: Synthesis and implications for hail growth and suppression. *Mon. Wea. Rev.,* **104,** 603–610.

Byers, H. R., and R. R. Braham Jr., 1949: *The Thunderstorm.* U.S. Government Printing Office, Washington, DC, 287 pp.

Chandrasekar, V., and R. J. Keeler, 1993: Antenna pattern analysis and measurements for multiparameter radars. *J. Atmos. Oceanic Technol.,* **10,** 674–683.

Cotton, W. R., and R. A. Anthes, 1989: *Storm and Cloud Dynamics.* Academic Press, 881 pp.

Cressman, G. P., 1959: An operational objective analysis system. *Mon. Wea. Rev.,* **87,** 367–374.

Dodge, J., J. Arnold, G. Wilson, J. Evans, and T. T. Fujita, 1986: The Cooperative Huntsville Meteorological Experiment (COHMEX). *Bull. Amer. Meteor. Soc.,* **67,** 417–419.

Doviak, R. J., and D. S. Zrnic, 1993: *Doppler Radar and Weather Observations.* Academic Press, 562 pp.

Dye, J. E., C. A. Knight, V. Toutenhoofd, and T. W. Cannon, 1974: The mechanism of precipitation formation in northeastern Colorado cumulus. III. Coordinated microphysical and radar observations and summary. *J. Atmos. Sci.,* **31,** 2152–2159.

El-Magd, A., V. Chandrasekar, V. N. Bringi, and W. Strapp, 2000: Multiparameter radar and in situ aircraft observation of graupel and hail. *IEEE Trans. Geosci. Remote Sens.,* **38,** 570–578.

Fujita, T. T., and P. G. Black, 1988: Monrovia microburst of 20 July 1986: A study of SST. Preprints, *15th Conf. on Severe Local Storms,* Baltimore, MD, Amer. Meteor. Soc., 380–383.

Goodman, S. J., D. E. Buechler, and P. D. Wright, 1988: Lightning and precipitation history of a microburst-producing storm. *Geophys. Res. Lett.,* **15,** 1185–1188.

Hall, M. P. M., S. M. Cherry, J. W. F. Goddard, and G. R. Kennedy, 1980: Raindrop sizes and rainfall rate measured by dual polarization radar. *Nature,* **285,** 195–198.

Herzegh, P. H., and R. E. Carbone, 1984: The influence of antenna illumination function characteristics on differential reflectivity measurements. Preprints, *22d Conf. on Radar Meteorology,* Zurich, Switzerland, Amer. Meteor. Soc., 281–286.

——, and A. R. Jameson, 1992: Observing precipitation through dual-polarization radar measurements. *Bull. Amer. Meteor. Soc.,* **73,** 1365–1374.

Hobbs, P. V., and A. L. Rangno, 1985: Ice particle concentrations in clouds. *J. Atmos. Sci.,* **42,** 2523–2549.

Holler, H., V. N. Bringi, J. Hubbert, M. Hagen, and P. F. Meischner, 1994: Life cycle and precipitation formation in a hybrid-type hailstorm revealed by polarimetric and Doppler radar measurements. *J. Atmos. Sci.,* **51,** 2500–2522.

Houghton, H. G., 1968: On precipitation mechanisms and their artificial modification. *J. Appl. Meteor.,* **7,** 851–859.

Houze, R. A., Jr., 1993: *Cloud Dynamics.* Academic Press, 573 pp.

——, 1997: Stratiform precipitation in regions of convection: A meteorological paradox? *Bull. Amer. Meteor. Soc.,* **78,** 2179–2196.

Hubbert, J., V. N. Bringi, and L. D. Carry, 1998: CSU-CHILL polarimetric radar measurements from a severe hailstorm in eastern Colorado. *J. Appl. Meteor.,* **37,** 749–775.

Husson, D., and Y. Pointin, 1989: Quantitative estimation of the hailfall intensity with a dual polarization radar and a hailpad network. Preprints, *24th Conf. on Radar Meteorology,* Tallahassee, FL, Amer. Meteor. Soc., 318–321.

Illingworth, A. J., J. W. F. Goddard, and S. M. Cherry, 1987: Polar-

ization radar studies in precipitation development in convective storms. *Quart. J. Roy. Meteor. Soc.,* **113,** 469–489.

Jameson, A. R., and D. B. Johnson, 1990: Cloud microphysics and radar. *Radar in Meteorology,* D. Atlas, Ed., Amer. Meteor. Soc., 323–340.

——, M. J. Murphy, and E. P. Krider, 1996: Multiple-parameter radar observations of isolated Florida thunderstorms during the onset of electrification. *J. Appl. Meteor.,* **35,** 343–354.

Keenan, T. D., B. Ferrier, and J. Simpson, 1994: Development and structure of a maritime continent thunderstorm. *Meteor. Atmos. Phys.,* **53,** 185–222.

Kingsmill, D. E., 1991: An observational study of the internal structure of airmass thunderstorms. Ph.D. dissertation, University of California, Los Angeles, 117 pp.

——, and R. M. Wakimoto, 1991: Kinematic, dynamic, and thermodynamic analysis of a weakly sheared severe thunderstorm over northern Alabama. *Mon. Wea. Rev.,* **119,** 262–297.

Leitao, M. J., and P. A. Watson, 1984: Application of dual linearly polarized radar data to prediction of microwave path attenuation at 10–30 GHz. *Radio Sci.,* **19,** 209–221.

Liu, H., and V. Chandrasekar, 2000: Classification of hydrometeors based on polarimetric radar measurements: Development of fuzzy logic and neuro-fuzzy systems, and in situ verification. *J. Atmos. Oceanic Technol.,* **17,** 140–164.

Oye, D., and M. Case, 1995: REORDER: A program for gridding radar data. Research Data program, Atmospheric Technology Division, National Center for Atmospheric Research, Boulder, CO.

Petersen, W. A., and Coauthors,1999: Mesoscale and radar observations of the Fort Collins flash flood of 28 July 1997. *Bull. Amer. Meteor. Soc.,* **80,** 191–216.

Raymond, D. J., and A. M. Blyth, 1986: A stochastic mixing model for nonprecipitating cumulus clouds. *J. Atmos. Sci.,* **43,** 2708–2718.

Rinehart, R. E., 1991: *Radar for Meteorologists.* 2d ed. University of North Dakota, 334 pp. [Available from Department of Atmospheric Sciences, University of North Dakota, Grand Forks, ND 58202.]

Rogers, R. R., and M. K. Yau, 1989: *A Short Course in Cloud Physics.* 3d ed. Pergamon Press, 293 pp.

Saunders, P. M., 1965: Some characteristics of tropical marine showers. *J. Atmos. Sci.,* **22,** 167–175.

Seliga, T. A., and V. N. Bringi, 1976: Potential use of radar reflectivity at orthogonal polarizations for measuring precipitation. *J. Appl. Meteor.,* **15,** 69–76.

Smith, P. L., D. J. Musil, A. G. Detwiller, and R. Ramachandran, 1999: Observations of mixed-phase precipitation within a CaPE thunderstorm. *J. Appl. Meteor.,* **38,** 145–155.

Straka, J. M., and D. S. Zrnic, 1993: An algorithm to deduce hydrometeor types and contents from multi-parameter radar data. Preprints, *26th Conf. on Radar Meteorology,* Norman, OK, Amer. Meteor. Soc., 513–515.

——, ——, and A. V. Ryzhkov, 2000: Bulk hydrometeor classification and quantification using polarimetric radar data: Synthesis of relations. *J. Appl. Meteor.,* **39,** 1341–1372.

Tuttle, J. D., V. N. Bringi, H. D. Orville, and F. J. Kopp, 1989: Multiparameter radar study of a microburst: Comparison with model results. *J. Atmos. Sci.,* **46,** 601–620.

Vivekanandan, J., D. S. Zrnic, S. M. Ellis, R. Oye, A. V. Ryzhkov, and J. Straka, 1999: Cloud microphysics retrieval using S-band polarization radar measurements. *Bull. Amer. Meteor. Soc.,* **80,** 381–388.

Wakimoto, R. M., and V. N. Bringi, 1988: Dual-polarization observations of microbursts associated with intense convection: The 20 July storm during the MIST project. *Mon. Wea. Rev.,* **116,** 1521–1539.

Wilson, J. W., and D. Reum, 1988: The flare echo: Reflectivity and velocity signature. *J. Atmos. Oceanic Technol.,* **5,** 197–205.

Woodward, B., 1959: The motion in and around isolated thermals. *Quart. J. Roy. Meteor. Soc.,* **85,** 144–151.

Yuter, S. E., and R. A. Houze Jr., 1995a: Three-dimensional kinematic and microphysical evolution of Florida cumulonimbus. Part I: Spatial distribution of updrafts, downdrafts, and precipitation. *Mon. Wea. Rev.,* **123,** 1921–1940.

——, and ——, 1995b: Three-dimensional kinematic and microphysical evolution of Florida cumulonimbus. Part II: Frequency distribution of vertical velocity, reflectivity, and differential reflectivity. *Mon. Wea. Rev.,* **123,** 1941–1963.

——, and ——, 1995c: Three-dimensional kinematic and microphysical evolution of Florida cumulonimbus. Part III: Vertical mass transport, mass divergence, and synthesis. *Mon. Wea. Rev.,* **123,** 1964–1983.